VYSOKÉ UČENÍ TECHNICKÉ V BRNĚ
BRNO UNIVERSITY OF TECHNOLOGY

FAKULTA STROJNÍHO INŽENÝRSTVÍ
FACULTY OF MECHANICAL ENGINEERING

ÚSTAV FYZIKÁLNÍHO INŽENÝRSTVÍ
INSTITUTE OF PHYSICAL ENGINEERING

MAGNETOOPTICKÁ CHARAKTERIZACE MATERIÁLŮ PRO SPINTRONIKU
MAGNETO-OPTICAL INVESTIGATION OF SPINTRONIC MATERIALS

BAKALÁŘSKÁ PRÁCE
BACHELOR'S THESIS

AUTOR PRÁCE — **Libor Vojáček**
AUTHOR

VEDOUCÍ PRÁCE — **M.Sc. Jon Ander Arregi Uribeetxebarria**
SUPERVISOR

BRNO 2019

VYSOKÉ UČENÍ TECHNICKÉ V BRNĚ
FAKULTA STROJNÍHO INŽENÝRSTVÍ

Zadání bakalářské práce

Ústav:	Ústav fyzikálního inženýrství
Student:	**Libor Vojáček**
Studijní program:	Aplikované vědy v inženýrství
Studijní obor:	Fyzikální inženýrství a nanotechnologie
Vedoucí práce:	**M.Sc. Jon Ander Arregi Uribeetxebarria**
Akademický rok:	2018/19

Ředitel ústavu Vám v souladu se zákonem č.111/1998 o vysokých školách a se Studijním a zkušebním řádem VUT v Brně určuje následující téma bakalářské práce:

Magnetooptická charakterizace materiálů pro spintroniku

Stručná charakteristika problematiky úkolu:

Magnetooptické jevy umožňují rychlé určení magnetických vlastností tenkých vrstev s vysokou citlivostí. Bakalářská práce se zaměří na návrh a sestavení magnetooptického elipsometru s využitím fotoelastického fázového modulátoru. Zařízení bude testováno na magnetických tenkých vrstvách s cílem určení magnetické anizotropie v závislosti na proměnných vnějších parametrech, například teplotě.

Cíle bakalářské práce:

1. Rešerše současného stavu poznání.
2. Návrh a sestavení zařízení pro měření magnetooptického Kerrova Jevu s využitím modulace vstupní polarizace světla.
3. Testování zařízení na modelových systémech tenkých vrstev a nanostruktur.

Seznam doporučené literatury:

BLUNDELL, S., Magnetism in Condensed Matter. Oxford University Press, New York, (2001).

QIU, Z. Q. a BADER, S. D., Surface magneto-optic Kerr effect. Review Scientific Instruments, vol. 71, pp. 1243, DOI: 10.1063/1.1150496, (2000).

VAVASSORI, P., Polarization modulation technique for magneto-optical quantitative vector magnetometry. Applied Physics Letters, vol. 77, pp. 1605, DOI: 10.1063/1.1310169, (2000).

STAMM, C. et al., Magneto-Optical Detection of the Spin Hall Effect in Pt and W Thin Films. Physical Review Letters, vol. 119, pp. 087203, DOI: 10.1103/PhysRevLett.119.087203, (2017).

Termín odevzdání bakalářské práce je stanoven časovým plánem akademického roku 2018/19

V Brně, dne

L. S.

prof. RNDr. Tomáš Šikola, CSc. ředitel ústavu	doc. Ing. Jaroslav Katolický, Ph.D. děkan fakulty

Abstrakt
Magnetooptický Kerrův jev představuje užitečný nástroj pro zkoumání magnetických vlastností kovových povrchů. Jeho využití při měření procesu přepínání magnetizace vnějším magnetickým polem nám může poskytnout cennou informaci o magnetické anizotropii zkoumané látky. V předložené práci se zabýváme teoretickými aspekty procesu přepínání magnetizace a změny polarizace světla při odrazu od magnetických povrchů. Dále je popsána optická sestava založená na modulaci polarizace světla schopná měřit magneto-optické veličiny s vysokou citlivostí. Tento přístroj byl sestaven modifikací již existující, podobné optické sestavy. Funkčnost zařízení byla ověřena měřeními na tenkých magnetických vrstvách. Získaná data pomáhají odhalit vlastnosti tenkých metamagnetických vrstev z FeRh, materiálu s potenciálními aplikacemi pro spintroniku.

Summary
The magneto-optical Kerr effect is a useful tool for accessing the magnetic properties of metallic surfaces. The magnetization reversal process controlled by an external applied field and magneto-optically measured can give us information about the anisotropic properties of magnetic systems. In the presented work, we review the theoretical aspects of magnetization reversal and the changes of light polarization upon reflection from a magnetized medium. Description of a functional, high-sensitivity magneto-optical setup based on the polarization modulation technique is given. The apparatus was assembled by modifying an already existing similar setup. Measurements on thin-film magnetic layers prove its functionality and reveal the properties of metamagnetic thin films from FeRh, which is a material with potential applications in spintronics.

Klíčová slova
magnetooptika, MOKE, Kerrův jev, Stonerův-Wohlfarthův model, magnetická anizotropie, FeRh, fázová přeměna

Keywords
magneto-optics, MOKE, Kerr effect, Stoner-Wohlfarth model, magnetic anisotropy, FeRh, phase transition

VOJÁČEK, Libor. *Magnetooptická charakterizace materiálů pro spintroniku.* Brno, 2019. 51 s. Bakalářská práce. Vysoké učení technické v Brně. Fakulta strojního inženýrství. Vedoucí práce Jon Ander ARREGI URIBEETXEBARRIA.

Prohlašuji, že jsem diplomovou práci *Magnetooptická charakterizace materiálů pro spintroniku* vypracoval samostatně pod vedením M.Sc. Jona Andera Arregiho, s použitím materiálů uvedených v seznamu literatury.

Libor Vojáček

Děkuji z celého srdce svým rodičům, kteří mě podporovali jak při psaní této práce, tak během celého studia. Děkuji svému vedoucímu M.Sc. Jonimu Arregimu především za všechen čas a péči, kterou mi věnoval, a také za přípravu měřených vzorků a jejich charakterizaci pomocí vibrační magnetometrie. Chtěl bych poděkovat Ing. Vojtěchu Uhlířovi, Ph.D. za to, že vytvořil prostor pro produktivní bádání. Mé díky patří Bc. Ondřeji Wojewodovi a Ing. Lukáši Flajšmanovi, na jejichž práci jsem stavěl a jejichž rady mi byly velkou pomocí. V neposlední řadě děkuji Janu Hajdučkovi za změření 26 nm vrstvy FeRh pomocí vibrační magnetometrie. Část práce byla provedena za podpory výzkumné infrastruktury CEITEC Nano (ID LM2015041, MŠMT, 2016–2019) , CEITEC Vysoké učení technické v Brně.

Libor Vojáček

Contents

Introduction

In 1985, Mark Johnson and Robert H. Silsbee discovered coupling between electron charge and its spin arising at an interface between a ferromagnet and a paramagnet: "a magnetic current can be created from an electric current, but more important, a nonequilibrium magnetization in a paramagnet can be detected as an electric voltage" [1]. This discovery marked the beginning of the field of *spintronics*. Three years later, Albert Fert and Peter Grünberg discovered that the sandwich structures of ferromagnetic and non-magnetic metallic layers show an unusually high (5%–20%) increase of resistance [2]. The increase arises, when the two ferromagnetic (FM) layers which were initially magnetized along the same direction are forced to have their magnetic moments antiparallel to each other. IBM exploited their discovery to make a magnetic sensor used as a read head in hard disk drives. This contributed to an increase of data storage density by 3 orders of magnitude between years 1991 and 2003 [2]. Even higher change in resistance with changing external magnetic field was measured in 1995 by replacing the non-magnetic metallic layer by an insulator, letting the electrons tunnel through. This discovery was commercialized by Seagate in 2005 [3]. The magnetic random access memory (MRAM) is based on this same magnetic tunnel junction [4]. The memory has a potential to become the "universal memory" [2]—useful as both a large data storage and a fast execution RAM. There has also been an extensive discussion on the use of spintronic-based memory cells for "processing-in-memory" computational approaches and its implementation as neural network accelerators [5].

Recently, a non-volatile type of memory based on the *antiferromagnetic* CuMnAs compound was realized [6]. The driving force for the magnetization reversal in this case is not an external magnetic field, but an electric current, which creates strong internal magnetic fields due to the special structure of the CuMnAs lattice. Since the material is antiferromagnetic (AF), it is insensitive to typical magnetic field perturbations and produces no external magnetic field.

There is a broad range of materials with room-temperature AF order, such as the near-equiatomic FeRh alloy. Additional to its AF ordering, after heating the material above $\sim$ 90°C, its magnetic order changes from AF to FM as a result of a first-order phase transition [7].

To investigate the magnetic properties of thin magnetic layers, the magneto-optical Kerr effect (MOKE) can be utilized [8–10]. In Chapter 1 of the presented thesis, we introduce the process of magnetization reversal and show how it can be used to study the magnetic anisotropy. Chapter 2 discusses the theoretical bases for description of the interaction of polarized light with a magnetic environment in the framework of electromagnetic theory. In Chapter 3, an experimental apparatus capable of measuring magnetic properties by reflection of polarized light is presented, and Chapter 4 demonstrates its usefulness via measurements of the magnetic anisotropy of Co and FeRh thin film layers.

1. Magnetism

According to classical physics, no spontaneous magnetization in a material should exist. This is stated in the *Bohr-van Leeuwen theorem* [11, Sec. 1.2.2]. To explain why some materials actually are magnetic, the introduction of quantum mechanical *spin* is needed and it is necessary to use quantum mechanical methods, which results in difficult calculations. Usually though, an approximate solution is enough. So for simulating real-life magnetism problems, the micromagnetic theory is often used.

1.1. Micromagnetic theory

The micromagnetic approach gives a mathematical tool for mesoscopic[1] simulations. The theory is not concerned with individual atomic magnetic moments [12], which change discretely with position, instead it treats the magnetization $\boldsymbol{M}(\boldsymbol{r})$ as a continuously varying function. It also assumes that the magnitude $|\boldsymbol{M}| \equiv M_s$, called the *spontaneous magnetization*, is position independent in a given material: only the orientation of $\boldsymbol{M}$ changes. The starting point for every calculation is expressing the Helmholtz free energy E. By finding the local minimum of E, we find the stable orientation for $\boldsymbol{M}$—the magnetization always adjusts itself to minimize the energy function. The choice of terms that one includes into E determines the properties one is able to account for.

The total free energy E_{tot} usually contains several contributions [13, chapter 7]

$$E_{tot} = E_{ex} + E_d + E_a + E_Z + E_{stress} + E_{ms}\,, \tag{1.1}$$

which are the exchange, demagnetizing, anisotropy, Zeeman, stress and magnetostriction energies, respectively.

The first three terms are always present in a ferromagnet:

1. ***The exchange energy***

$$E_{ex} = \int A \left(\frac{\nabla \boldsymbol{M}}{M_s} \right)^2 \mathrm{d}^3 r \tag{1.2}$$

   acts to align the neighboring magnetic moments in one direction (ferromagnetism), or in alternating directions (antiferromagnetism), depending on the sign of the *exchange stiffness* A.

[1] Mesoscopic structures are on the order of $\sim$ 100–1000 nm.

2. ***The demagnetizing energy*** E_d increases when $\boldsymbol{M}$ points in or out of a surface boundary. This gives rise to virtual *magnetic charges* that create the *demagnetizing field* $\boldsymbol{H}_d$ which tends to align the magnetization tangent to the surface. Inside the material, the magnetic charges can also arise if the magnetization is divergent: $\boldsymbol{\nabla} \cdot \boldsymbol{M} \neq 0$. The competition between this interaction and the exchange is responsible for the appearance of magnetic domains in ferromagnetic materials.

3. ***The magnetocrystalline anisotropy energy*** E_a gives a preferential magnetization direction in a crystal. This preferential direction is called the *easy axis* (EA) and there can be multiple of them. In a cubic crystal, the anisotropy energy can be expressed as [14]

$$E_a = K_1(m_x^2 m_y^2 + m_x^2 m_z^2 + m_y^2 m_z^2) + K_2(m_x^2 m_y^2 m_z^2)\,, \tag{1.3}$$

   where K_1 and K_2 are cubic magnetocrystalline anisotropy constants and m_x, m_y and m_z are the respective *direction cosines* of magnetization.

4. ***The Zeeman energy*** E_Z is lowest when $\boldsymbol{M}$ is aligned parallel to an external magnetic field

$$E_Z = -\mu_0 \int \boldsymbol{M} \cdot \boldsymbol{H}_{ext} \mathrm{d}^3 r\,. \tag{1.4}$$

5. The energy terms due to **stress** E_{stress} and ***magnetostriction*** E_{ms} are usually small and request the coupling between mechanical and magnetic properties of the material.

1.2. Magnetization reversal

We can flip $\boldsymbol{M}$ to $-\boldsymbol{M}$ by applying strong enough external field. This is called *magnetization reversal*. The response of $\boldsymbol{M}$ to $\boldsymbol{H}_{ext}$ depends on the previous magnetization state.[2] This is because there are usually multiple *local* energy minima of E_{tot} (1.1), so the system will settle into a *metastable* state that does not have to be the state of *global* energy minimum—to reach the global minimum, it would have to overcome an energy barrier.

Fig. 1.1 shows a hysteresis curve: the component of $\boldsymbol{M}$ pointing along $\boldsymbol{H}_{ext}$ and denoted as $M_\parallel$ plotted as a function of the external field magnitude H_{ext}. The highest value $M_\parallel$ can reach is the saturation magnetization M_s. The field for which the magnetization vanishes ($M_\parallel = 0$) is called the *coercive field* H_c. The value of $M_\parallel$ at zero applied field is called the *remanent magnetization* M_r.

There are multiple mechanisms involved in the magnetization reversal [13]. Imagine that at the beginning, the field is at its negative maximum and so the magnetization is at its negative saturation: $M_\parallel = -M_s$. In an anisotropic material with a preferred magnetization direction, increasing the field from its saturation state first results in a *coherent rotation*, where $\boldsymbol{M}$ slowly rotates toward one of the easy axes. This is part (1) in Fig. 1.1. For a sufficiently large sample, magnetic domains can arise. Increasing the field

[2] Magnets have memory, so to say.

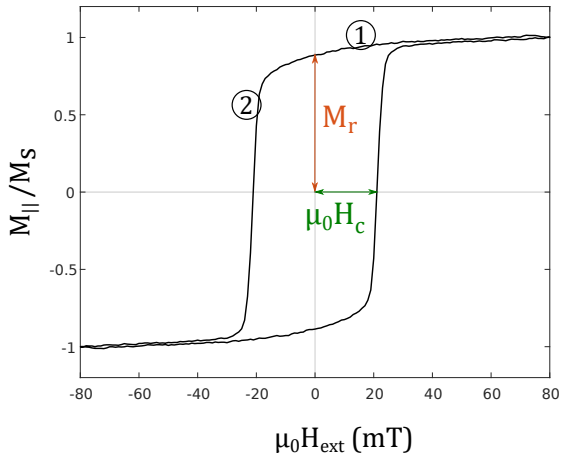

Figure 1.1: Magnetic hysteresis curve. M_s is the saturation magnetization, $\mu_0 H_c$ the coercive field and M_r the remanent magnetization. The coherent rotation region is denoted by number 1, number 2 denotes where the domain walls move and new ones nucleate. Inspired by [13].

to positive values, domains with their $\boldsymbol{M}$ aligned along $\boldsymbol{H}_{ext}$ will increase in size. This process is called the *domain wall motion*. New domains with their $\boldsymbol{M}$ oriented along $\boldsymbol{H}_{ext}$ will *nucleate*, mostly at the surface or at the material deffects.

A simple and analytically soluble model for magnetization reversal was developed in 1948 by Elmer C. Stoner and Erich P. Wohlfarth [15].

1.3. Stoner-Wohlfarth model

Let's suppose our magnetic system is described by a single vector $\boldsymbol{M}$, homogeneous in the whole volume. This is true for a rotationally symmetric ellipsoid that is small enough to be composed of a single magnetic domain—Fig. 1.2 b). Namely an infinite plane can be thought of as a limiting case of an ellipsoid, with two of its axes stretching to infinity. The Stoner-Wohlfarth (SW) model considers only two energy contributions[3]: the anisotropy energy E_A and the Zeeman energy E_Z [16]

$$E = E_A + E_Z \,. \tag{1.5}$$

The anisotropy energy is rather empirical and it can take various forms. Two of these forms, used later in the thesis, are presented in the next two sections.

1.3.1. Uniaxial anisotropy

If there is only one easy axis, the material is said to have a uniaxial anisotropy. Uniaxial anisotropy is characteristic for hexagonal materials. The anisotropy energy term can be expressed as

$$E_A = K_u \sin^2 \vartheta \,, \tag{1.6}$$

[3]The exchange energy is present, but it is a constant, because we assume $\boldsymbol{M}$ to be homogeneous.

where K_u is the *uniaxial anisotropy constant*, ϑ is the angle between $\boldsymbol{M}$ and the easy axis (Fig. 1.2 c)), and α is the angle between $\boldsymbol{H}$ and the EA; both angles lie in the same plane. We can define the *uniaxial anisotropy field*

$$H_u \equiv 2K_u/\mu_0 M_s \,. \tag{1.7}$$

A polarplot of the uniaxial energy profile is the black curve in Fig. 1.2 c).

Suppose that the saturation magnetization M_s and the uniaxial anisotropy constant K_u of the sample are known and the direction of the applied field α and its magnitude H are given by the experiment. We can change H from its negative maximum to its positive maximum and back to negative, and for every applied field we find the magnetization direction $\theta = \theta^*$ that minimizes the energy density (1.5). This can be done very efficiently using a numerical iterative method described in Appendix A. The magnetization component parallel to $\boldsymbol{H}$, $M_\parallel = M_s \cos(\alpha - \theta^*)$, is plotted in Fig. 1.2 a) for different directions of $\boldsymbol{H}_{ext}$. In Fig. 1.2 c) there is a complete magnetization reversal process. Red points indicate the magnetization direction when increasing the field, which is applied at 45° from the easy axis. In the beginning, $\boldsymbol{H}$ is in its negative maximum and $\boldsymbol{M}$ lies almost exactly along $\boldsymbol{H}$. This starting point is indicated by the red square. The field gradually increases, which guides the magnetization to coherently rotate closer to the easy axis and align with it when H reaches zero. When the field increases to certain positive value the magnetization abruptly switches (dashed red line). The coherent rotation then continues until $\boldsymbol{H}$ reaches its positive maximum (blue square). When decreasing the field back to its negative maximum (blue dots and line), a similar rotation-switch-rotation process happens, but $\boldsymbol{M}$ does not follow exactly the same path as before: the behavior is *hysteretic*[4].

1.3.2. Fourfold anisotropy

In systems with two easy axes (perpendicular to each other), we are talking about the *fourfold anisotropy*. This type is characteristic for materials with a cubic lattice. The anisotropy energy can be expressed as

$$E_A = K_1 \sin^2\theta \cos^2\theta \,, \tag{1.8}$$

where K_1 is the fourfold energy coefficient. This term can be accompanied by a small uniaxial contribution. We also define the *fourfold anisotropy field*

$$H_1 \equiv 2K_1/\mu_0 M_s \,. \tag{1.9}$$

Magnetization reversal for this case is shown in Fig. 1.3. When applying the field near to a *hard axis*—Fig. 1.3 b) and the yellow curve in Fig. 1.3 a)—there are two switches in the rotation-switch-rotation-switch-rotation process.

[4]Except for the case of $\boldsymbol{H}$ applied along hard axis.

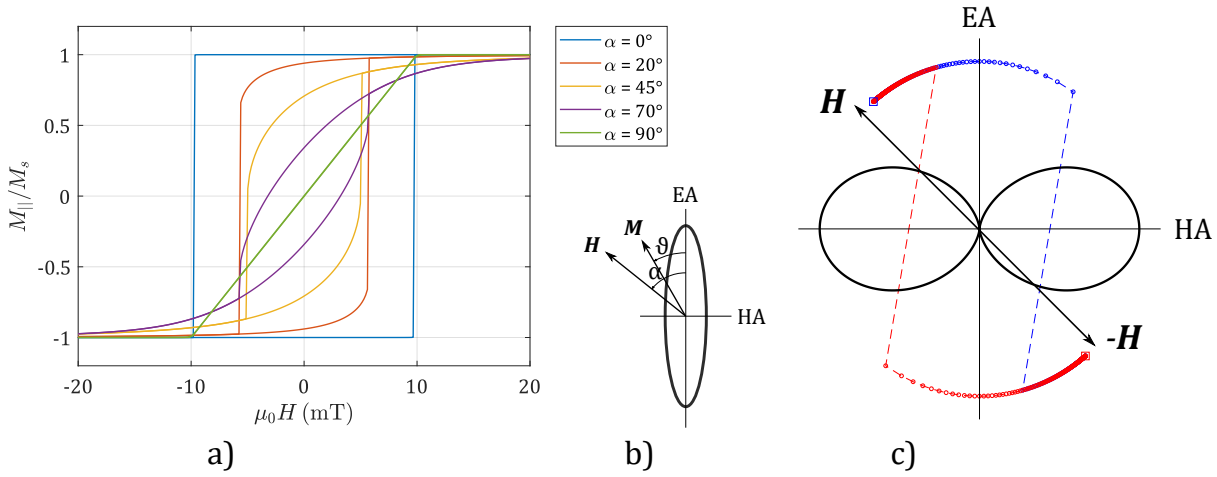

Figure 1.2: a) Hysteresis loops numerically calculated using the Stoner-Wohlfarth model for different external field orientations α. The uniaxial anisotropy field is chosen $H_u =$ $= -10$ mT. b) A Stoner particle: an ellipsoid object with uniform magnetization in its whole volume. c) The uniaxial anisotropy energy profile in polar coordinates (black curve). The endpoints of $\boldsymbol{M}$ during a magnetization reversal process with field applied at 45° from the EA: the red points are for the increasing-field half of the reversal, the blue points for the decreasing-field part. (Some of the blue points are covered by the red ones.) Projection of these points into the $\boldsymbol{H}$ direction is the yellow hysteresis curve in a).

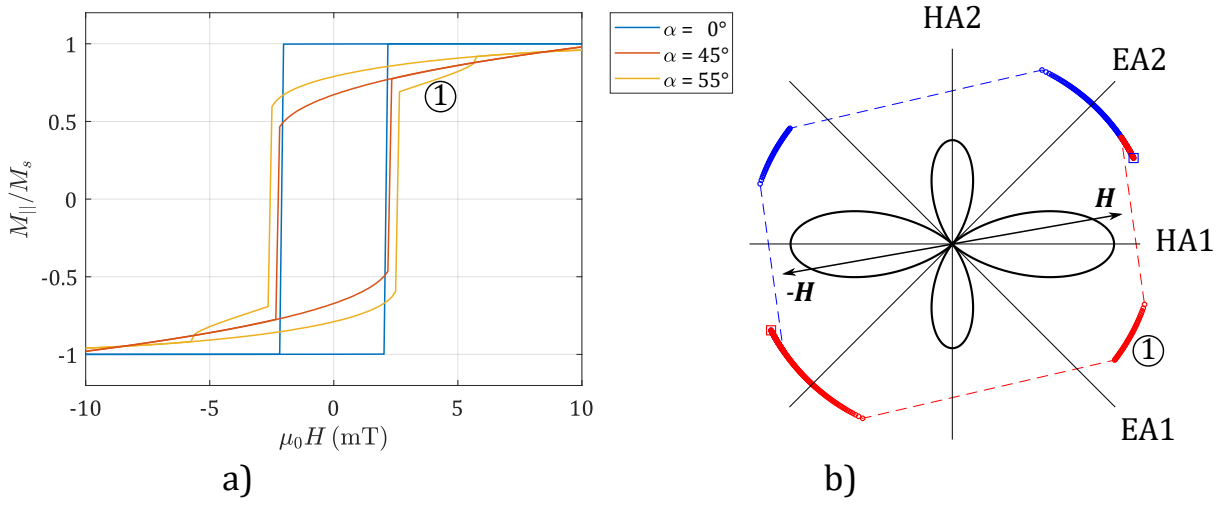

Figure 1.3: a) Hysteresis loops for a fourfold anisotropy with $H_1 = -10$ mT with a small uniaxial contribution with $H_u = -1$ mT. b) The anisotropy energy profile (black curve). The endpoints of $\boldsymbol{M}$ in the magnetization reversal process when $\boldsymbol{H}$ is applied at $\alpha =$ $= 55°$ from EA1 (red and blue points). The fourfold anisotropy magnetization switching is characterized by the second rotation part denoted by 1.

2. Magneto-optics

Michael Faraday strongly believed that all forces in the nature—gravitation, electricity, magnetism and even light—are connected [17]. In 1845 he discovered that light and magnetism truly relate to each other. He found out that the azimuth of a linearly polarized light slightly rotates after the light has passed through a piece of flint glass that was placed in an electromagnet. This effect of magnetized matter on the polarization of light was named *the Faraday rotation*. In his paper from 1846 he further explains: "The magnetic forces do not act on the ray of light directly and without the intervention of matter, but through the mediation of the substance in which they and the ray have a simultaneous existence." Due to this, we are able to investigate the material properties with a polarized light.

Although groundbreaking, Faraday's discovery cannot be used for investigation of metals because of their high absorption. In 1876 however, Reverend John Kerr observed a similar polarization change in a light reflected from a polished electromagnet pole [18]. This phenomenon is called the *magneto-optical Kerr effect* (MOKE).

With MOKE it is possible to measure magnetic properties of metals, even metallic layers as thin as few atomic monolayers [9]. The method is quick, nondestructive, and also quite accessible as only a few optical components are needed. If the light is focused, individual micro- and nanostructures can be probed for their magnetic properties, even obtaining the whole magnetization direction vector [19]. Magnetization processes as fast as $\sim$ 10 femtoseconds can be studied by the "pump-probe" techniques using the *time-resolved MOKE* [20]. Very recently, spintronic phenomena such as the spin Hall effect in metals, has also been detected using MOKE [21].

In this chapter we will introduce the electromagnetic theory and describe light as an electromagnetic wave. We will describe light polarization within the Jones formalism, which helps us compute the changes of polarization in optical systems. In Section 2.3 we will interconnect magnetization and light polarization via the electric permittivity tensor and state the formulas for Fresnel reflection coefficients in a magnetized matter. The last section introduces two widely used magneto-optical measurement methods.

2.1. Electromagnetic field

The electromagnetic theory, unified by James Clerk Maxwell in 1873, describes the interaction of electric and magnetic fields, and tells us how they are produced by charges and currents [22–24]. The action of the fields on a charged particle is then expressed by the Lorentz force.

The electric field is described by the *electric field* vector $\boldsymbol{E}$ and the *electric displacement* vector $\boldsymbol{D}$. While $\boldsymbol{E}$ is a measurable quantity, $\boldsymbol{D}$ is not, and it is only defined in terms of $\boldsymbol{E}$ as

$$\boldsymbol{D} \stackrel{\text{def}}{=} \varepsilon_0 \boldsymbol{E} + \boldsymbol{P}\,, \tag{2.1}$$

where $\varepsilon_0 = 8.854 \cdot 10^{-12}\,\mathrm{F{\cdot}m^{-1}}$ is the *permittivity of free space* and $\boldsymbol{P}$ is the *polarization*: the *electric dipole moment* per unit volume. Defining $\boldsymbol{D}$ allows us to work only with free-moving electric charges instead of electric charges as a whole.

In the simplest case the polarization $\boldsymbol{P}$ in a material is induced by the external electric field $\boldsymbol{E}$ and is proportional to it

$$\boldsymbol{P} = \varepsilon_0 \chi \boldsymbol{E}\,, \tag{2.2}$$

the constant of proportionality being the *electric susceptibility* χ times ϵ_0. We define the *relative permittivity*

$$\varepsilon_r \stackrel{\text{def}}{=} 1 + \chi\,, \tag{2.3}$$

and the *permittivity*

$$\varepsilon \stackrel{\text{def}}{=} \varepsilon_r \varepsilon_0\,. \tag{2.4}$$

Then we can write

$$\boldsymbol{D} = \varepsilon \boldsymbol{E}\,. \tag{2.5}$$

The relative permittivity ε_r is a material property. In an anisotropic media, it is quite possible that $\boldsymbol{P}$ does not lie along $\boldsymbol{E}$. In that case, for being able to describe $\boldsymbol{P}$ in terms of $\boldsymbol{E}$, the electric susceptibility χ has to be a second-rank tensor and the electric permittivity takes the form

$$\hat{\varepsilon} = \varepsilon_0 \begin{pmatrix} 1+\chi_{xx} & \chi_{xy} & \chi_{xz} \\ \chi_{yx} & 1+\chi_{yy} & \chi_{yz} \\ \chi_{zx} & \chi_{zy} & 1+\chi_{zz} \end{pmatrix}. \tag{2.6}$$

The magnetic field is also described by two quantities. Both are called the *magnetic field*, the first being the *B-field* $\boldsymbol{B}$ and the second being the *H-field* $\boldsymbol{H}$. B-field is a directly measurable quantity while H-field is not; it is only defined in terms of $\boldsymbol{B}$ as

$$\boldsymbol{B} = \mu_0(\boldsymbol{H} + \boldsymbol{M})\,, \tag{2.7}$$

where the *permeability of free space* $\mu_0 = 4\pi \cdot 10^{-7}\,\mathrm{H{\cdot}m^{-1}}$ and $\boldsymbol{M}$ is the *magnetization*: the *magnetic moment* per unit volume. In the simplest case, $\boldsymbol{M}$ is induced by the magnetic field $\boldsymbol{H}$ and is proportional to it

$$\boldsymbol{M} = \chi_m \boldsymbol{H}\,, \tag{2.8}$$

the constant of proportionality being the *magnetic susceptibility* χ_m. We define the *relative permeability*

$$\mu_r \stackrel{\text{def}}{=} 1 + \chi_m\,, \tag{2.9}$$

and the *permeability*

$$\mu \stackrel{\text{def}}{=} \mu_r \mu_0\,. \tag{2.10}$$

Then we can write

$$\boldsymbol{B} = \mu \boldsymbol{H}\,. \tag{2.11}$$

Just as χ and ε, χ_m and μ are generally second rank tensors (3×3 matrices).

The sources of the fields are electric charges and currents described by the *charge density* ϱ and the current density $\boldsymbol{j}$. Thanks to introducing the "auxiliary fields" $\boldsymbol{D}$ and $\boldsymbol{H}$, we are allowed to work only with the charges that move freely. The effect of *bound charges*[1] is included in $\boldsymbol{P}$ and $\boldsymbol{M}$ and thus in $\boldsymbol{D}$ and $\boldsymbol{H}$. Instead of ϱ and $\boldsymbol{j}$ then, we can use the *free charge density* ϱ_f and the *free current density* $\boldsymbol{j}_f$.

Maxwell equations

The Maxwell equations are the *Gauss's law*, the *Gauss's law for magnetic field*, the *Faraday's law* and the *Ampere's-Maxwell's law*

$$\boldsymbol{\nabla} \cdot \boldsymbol{D} = \varrho_f \,, \tag{2.12a}$$
$$\boldsymbol{\nabla} \cdot \boldsymbol{B} = 0 \,, \tag{2.12b}$$
$$\boldsymbol{\nabla} \times \boldsymbol{E} + \frac{\partial}{\partial t}\boldsymbol{B} = \boldsymbol{0} \,, \tag{2.12c}$$
$$\boldsymbol{\nabla} \times \boldsymbol{H} - \frac{\partial}{\partial t}\boldsymbol{D} = \boldsymbol{j}_f \,. \tag{2.12d}$$

Along with the *Lorentz force*

$$\boldsymbol{F}_L = q\boldsymbol{E} + q\boldsymbol{v} \times \boldsymbol{B} \tag{2.13}$$

which tells us the force exerted on charge q by external electric and magnetic fields, the Maxwell equations constitute the complete theory of electromagnetism.

Light as a plane wave

Light can be described as a wave of electromagnetic field. We inspect the propagation of an electromagnetic wave in an environment with no free charges and no free currents

$$\begin{aligned} \varrho_f &= 0 \,, \\ \boldsymbol{j}_f &= \boldsymbol{0} \,, \end{aligned} \tag{2.14}$$

in which the light propagates with a constant speed $v = c/n$—the speed of light in vacuum is exactly $c = 299\,792\,458\,\mathrm{m{\cdot}s^{-1}}$ and n is the *refractive index*.

[1] The bound charges are created by the electrons that are bound in atomic orbitals.

The wave equation

$$\begin{aligned} \boldsymbol{\nabla} \times (\boldsymbol{\nabla} \times \boldsymbol{E}) + \frac{1}{c^2}\mu_r \boldsymbol{\varepsilon_r} \frac{\partial^2 \boldsymbol{E}}{\partial t^2} = 0\,, \\ \boldsymbol{\nabla} \times (\boldsymbol{\nabla} \times \boldsymbol{B}) + \frac{1}{c^2}\mu_r \boldsymbol{\varepsilon_r} \frac{\partial^2 \boldsymbol{B}}{\partial t^2} = 0\,, \end{aligned} \tag{2.15}$$

for $\boldsymbol{E}$ can be obtained by performing the $\boldsymbol{\nabla}\times$ ("curl") operation to both sides of (2.12c) and substituting from (2.12d). To derive the equation for $\boldsymbol{B}$ apply $\boldsymbol{\nabla}\times$ to (2.12d) and substitute from (2.12c). One also uses the fact that $c^2 = 1/\mu_0\varepsilon_0$.

If $\varrho_f = 0$, $\boldsymbol{j}_f = \boldsymbol{0}$, it is convenient to use the mathematical identity

$$\boldsymbol{\nabla} \times (\boldsymbol{\nabla} \times \boldsymbol{E}) = \boldsymbol{\nabla}(\boldsymbol{\nabla} \cdot \boldsymbol{E}) - \boldsymbol{\nabla}^2 \boldsymbol{E} \tag{2.16}$$

and use (2.12a) with (2.12b) to obtain

$$\boldsymbol{\nabla}^2 \boldsymbol{E} = \frac{1}{v^2}\frac{\partial^2 \boldsymbol{E}}{\partial t^2}\,, \tag{2.17a}$$

$$\boldsymbol{\nabla}^2 \boldsymbol{B} = \frac{1}{v^2}\frac{\partial^2 \boldsymbol{B}}{\partial t^2}\,. \tag{2.17b}$$

The simplest solution to the wave equation is *a plane wave* [25, p. 24]. In complex representation

$$\boldsymbol{E} = \mathrm{Re}\left\{\boldsymbol{E}_0 \mathrm{e}^{-i(\omega t - \boldsymbol{k}\cdot\boldsymbol{r})}\right\}\,, \tag{2.18a}$$

$$\boldsymbol{B} = \mathrm{Re}\left\{\boldsymbol{B}_0 \mathrm{e}^{-i(\omega t - \boldsymbol{k}\cdot\boldsymbol{r})}\right\}\,, \tag{2.18b}$$

where $\boldsymbol{k}$ is the *wave vector*, ω is the *angular frequency* and $\boldsymbol{E}_0$ with $\boldsymbol{B}_0$ are complex vector amplitudes of the fields.

Note that thanks to the unique behaviour of exponential function $\frac{\mathrm{d}}{\mathrm{d}x}\mathrm{e}^{\alpha x} = \alpha \mathrm{e}^{\alpha x}$, the spatial derivatives (divergenece and curl) and the time derivative, when applied to the plane wave, simply become algebraic expressions

$$\begin{aligned} \boldsymbol{\nabla}\cdot &\longrightarrow i\boldsymbol{k}\cdot\,, \\ \boldsymbol{\nabla}\times &\longrightarrow i\boldsymbol{k}\times\,, \\ \frac{\partial}{\partial t} &\longrightarrow -i\omega\,. \end{aligned} \tag{2.19}$$

If we substitute the plane wave solution back to the Maxwell equations (2.12a)–(2.12d), we–learn that

$$\boldsymbol{k}\cdot\boldsymbol{E} = 0\,, \quad \boldsymbol{k}\cdot\boldsymbol{B} = 0\,, \quad \boldsymbol{E}\cdot\boldsymbol{B} = 0\,, \tag{2.20a}$$

$$B = \frac{E}{\mathrm{c}}\,. \tag{2.20b}$$

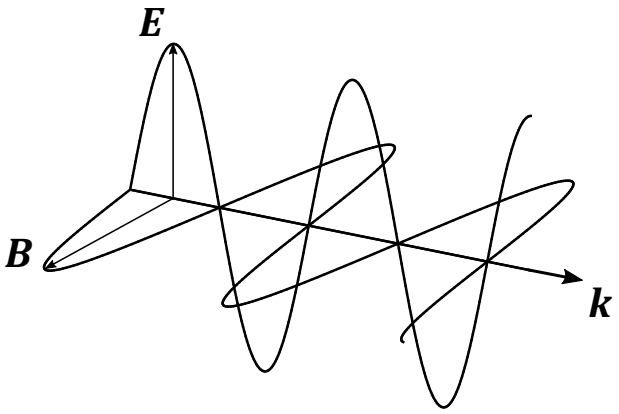

Figure 2.1: Plane wave of light. Vectors $\boldsymbol{E}$, $\boldsymbol{B}$ and $\boldsymbol{k}$ are perpendicular to each other.

This implies that all three vectors are orthogonal

$$\boldsymbol{E} \perp \boldsymbol{k}\,, \quad \boldsymbol{B} \perp \boldsymbol{k}\,, \quad \boldsymbol{E} \perp \boldsymbol{B}\,, \tag{2.21}$$

and thus light in free space is a transversal wave (Fig. 2.1). Together with Eq. (2.20b), it is also clear that once we calculate $\boldsymbol{E}$ for a known $\boldsymbol{k}$, we can easily obtain $\boldsymbol{B}$. By this argument from now on we express all the properties of propagating light by $\boldsymbol{E}$ alone.

Note that the plane wave is a solution to the wave equation only for *infinite* homogeneous media. In regions with boundaries, we can use it as an approximate solution [9, p. 29].

2.2. Polarized light

In this section we describe polarized light by the Jones formalism, point out the special cases of linear and circular polarization and show how to describe polarizing optical systems with 2x2 matrices. In the end, the complex Kerr angle will be defined as a quantity of interest in magneto-optical experimental efforts.

2.2.1. Jones vector

Let's choose our cartesian coordinate system such that the light is propagating in the z-direction, i.e. $\boldsymbol{k} = (0,\, 0,\, k)$. For a plane wave then [26, p. 173]

$$\boldsymbol{E} = \begin{pmatrix} E_{0x} \\ E_{0y}\mathrm{e}^{\mathrm{i}\delta} \\ 0 \end{pmatrix} \mathrm{e}^{\mathrm{i}(kz-\omega t)}\,, \tag{2.22}$$

where E_{0x} and E_{0y} are the amplitudes of $\boldsymbol{E}$ in the particular directions and δ is the phase difference between the x and y components.

Motivated by this expression, we describe the polarization state of light by the normalized *Jones vector* [25, 27]

$$\boldsymbol{J} = \frac{1}{\sqrt{E_{0x}^2 + E_{0y}^2}} \begin{pmatrix} E_{0x} \\ E_{0y}\mathrm{e}^{\mathrm{i}\delta} \end{pmatrix}\,. \tag{2.23}$$

We normalize the vector in the sense that the amplitude $|\boldsymbol{J}| = \sqrt{\boldsymbol{J}^\dagger \boldsymbol{J}} = 1$ and it is just a matter of convention (the † sign denotes the *Hermitian adjoint* [28, p. 146]).

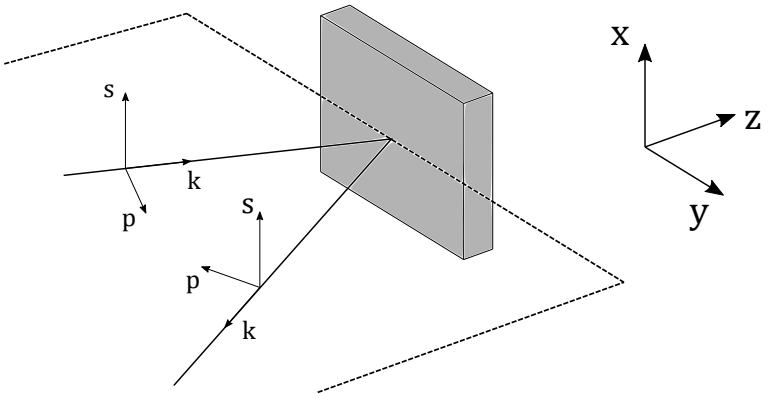

Figure 2.2: The static laboratory xyz coordinate system vs. the light coordinate system. The p-direction lies in the plane of incidence and the s-direction perpendicular to it. Both of them are perpendicular to $\boldsymbol{k}$.

A new coordinate system for light

Usually in physics, it is convenient to use a static *laboratory coordinate system*. In optics this is not true. The light changes its direction of propagation very often - every time it gets reflected or refracted. So it can happen that for example two polarizing filters are both facing the light beam in the same way (like in Fig. 2.7), but they are rotated with respect to each other as seen from the view of the laboratory reference frame. This means that mathematically they will be described in a different way, although their action on the light is precisely the same.

This is the reason for defining a new coordinate system, inextricably connected with the propagating light (Fig. 2.2). We define the s-direction (from german "senkrecht") to be perpendicular to the plane of incidence and the p-direction (from german "parallel") to be parallel to it. Both s and p are always perpendicular to $\boldsymbol{k}$.

From now on we will always use this new coordinate system when using the Jones vectors. Writing $\boldsymbol{J} = \begin{pmatrix} 1 \\ 0 \end{pmatrix}$ will mean that the light is fully polarized in s (not x) and writing $\boldsymbol{J} = \begin{pmatrix} 0 \\ 1 \end{pmatrix}$ will mean that the light is fully polarized in p (not y)

$$\boldsymbol{J}_s = \begin{pmatrix} 1 \\ 0 \end{pmatrix}, \quad \boldsymbol{J}_p = \begin{pmatrix} 0 \\ 1 \end{pmatrix}. \tag{2.24}$$

Linear and circular polarization

If both components of $\boldsymbol{J}$ are real, the polarization is said to be *linear*

$$\boldsymbol{J}_{lin.} = \begin{pmatrix} a \\ b \end{pmatrix}, \quad a,\, b \in \mathbb{R}\,. \tag{2.25}$$

It can be expressed as a linear combination of the s- and p-polarized plane waves (Fig. 2.3).

If the Jones vector takes one of the forms

$$\boldsymbol{J}_{LCP} = \frac{1}{\sqrt{2}} \begin{pmatrix} 1 \\ i \end{pmatrix}, \quad \boldsymbol{J}_{RCP} = \frac{1}{\sqrt{2}} \begin{pmatrix} 1 \\ -i \end{pmatrix}, \tag{2.26}$$

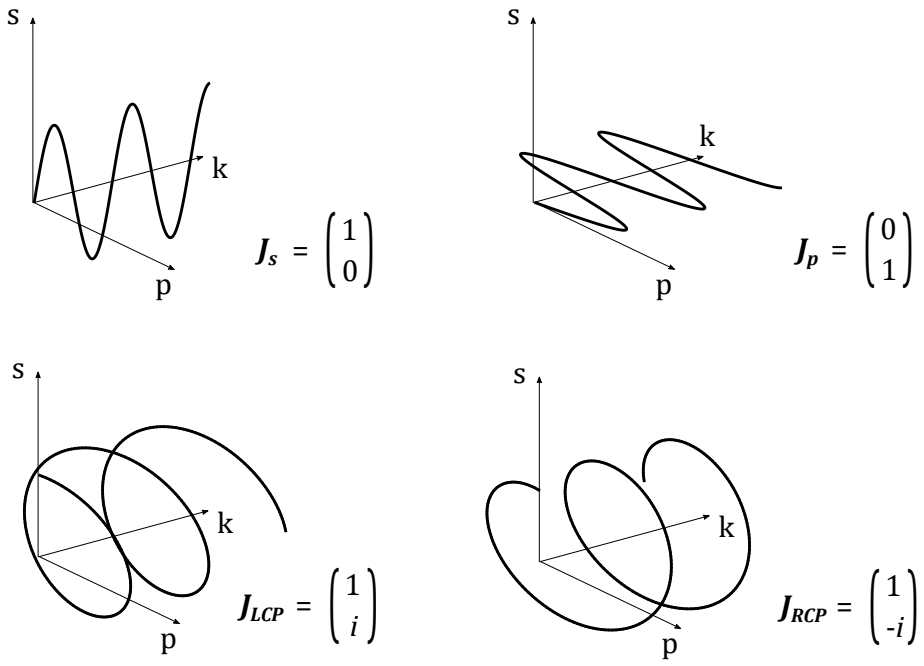

Figure 2.3: Linear and circular polarization. Both $\boldsymbol{J}_s$ with $\boldsymbol{J}_p$ and $\boldsymbol{J}_{RCP}$ with $\boldsymbol{J}_{LCP}$ form an orthogonal two-dimensional basis for describing the polarization of light in means of Jones formalism.

we are talking about the *left-circularly* (LCP) and *right-circularly* (RCP) polarized light (Fig. 2.3).

Note that $\boldsymbol{J}_{LCP}$ with $\boldsymbol{J}_{RCP}$ are orthogonal vectors

$$\boldsymbol{J}_{LCP}^{\dagger} \cdot \boldsymbol{J}_{RCP} = \begin{pmatrix} 1 & -\mathrm{i} \end{pmatrix} \begin{pmatrix} 1 \\ -\mathrm{i} \end{pmatrix} = 0\,, \tag{2.27}$$

just as $\boldsymbol{J}_p$ with $\boldsymbol{J}_s$.

So instead of s and p we could also use LCP and RCP as an *orthogonal basis* for description of polarized light.

2.2.2. Ellipsometric angles

In the most general case, the Jones vector takes the form of (2.23) and the polarization is said to be *elliptical* [25, p. 328]. That is because in a fixed point in space when looking at a plane perpendicular to $\boldsymbol{k}$, the endpoint of $\boldsymbol{E}$ will trace out an ellipse, as shown in Figure 2.6. This can be shown by taking the real part of (2.22) and eliminating time.

A usual form of $\boldsymbol{J}$ for ellipticaly polarized light is obtained after dividing (2.23) by E_{0x} and omitting the normalization. We also define the complex angle Φ

$$\boldsymbol{J}_{ell.} = \begin{pmatrix} 1 \\ \frac{E_{0y}}{E_{0x}} \mathrm{e}^{\mathrm{i}\delta} \end{pmatrix} \stackrel{\text{def}}{=} \begin{pmatrix} 1 \\ \Phi \end{pmatrix}. \tag{2.28}$$

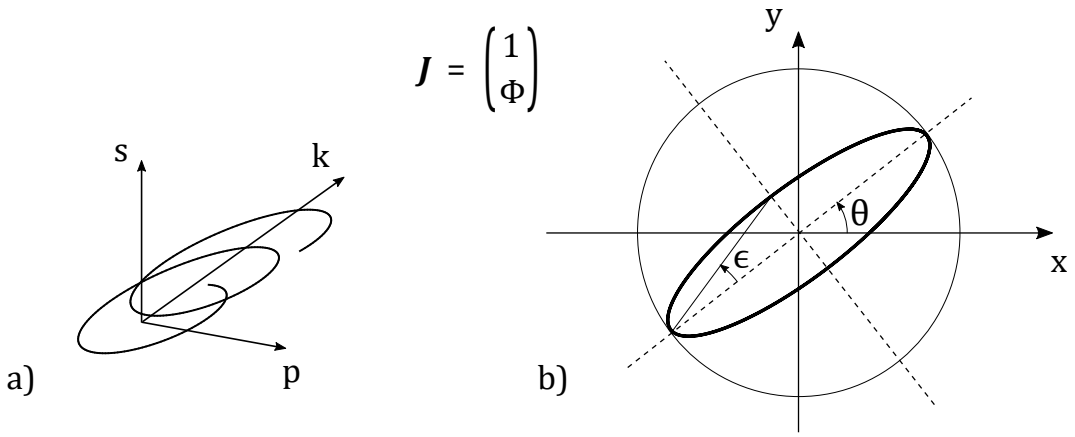

Figure 2.4: a) Ellipticaly polarized wave. b) Mathematical description of ellipse by the two parameters θ and ϵ.

In the complex angle Φ, two real angles θ and ϵ are hidden. These two angles are all we need to describe an ellipse[2] (Fig. 2.6). They are usually very small, of the order of 1 miliradian: $\theta \cong \epsilon \cong 1$ mrad.

The ellipticity ϵ is defined as

$$\tan \epsilon = \frac{E_{0y}}{E_{0x}}\,, \tag{2.29}$$

and *the rotation* θ is the angle between the ellipse major axis and the s direction.

Let us write the Jones vector for a non-rotated (left-circular) ellipse[3] and apply the rotation matrix [27, p. 4]

$$\begin{aligned} \boldsymbol{J}_{ell.} &= \begin{pmatrix} \cos\theta & -\sin\theta \\ \sin\theta & \cos\theta \end{pmatrix} \cdot \begin{pmatrix} 1 \\ \mathrm{i}\tan\epsilon \end{pmatrix} = \begin{pmatrix} \cos\theta - \mathrm{i}\sin\theta\cdot\tan\epsilon \\ \sin\theta + \mathrm{i}\cos\theta\cdot\tan\epsilon \end{pmatrix} \\ &\propto \begin{pmatrix} 1 \\ \frac{\tan\theta + \mathrm{i}\tan\epsilon}{1 - \mathrm{i}\tan\theta\cdot\tan\epsilon} \end{pmatrix} \approx \begin{pmatrix} 1 \\ \theta + i\epsilon \end{pmatrix}. \end{aligned} \tag{2.30}$$

We divided by the s component[4] and neglected all second and higher order terms in θ and ϵ, because they are small.

Comparing with Eq. (2.28), we find out that

$$\Phi \approx \theta + i\epsilon\,. \tag{2.31}$$

This is an important result. After expressing our optical system by the Jones formalism, introduced in the next section, and calculating the resultant polarization of light, we can always tell the two ellipsometric quantities θ and ϵ by dividing $\boldsymbol{J}$ by one of its components and using Eq. (2.31) along with (2.28).

[2]which has its major axis length equal to 1 for the sake of normalization
[3]It is just $\boldsymbol{J}_{LCP}$ with $J_p = \tan\epsilon$ insted of $J_p = 1$
[4]Because in this case J_s is much larger than J_p. If J_p was larger, we would divide by it.

2.2.3. Jones matrices

After introducing the Jones vector, we can conveniently describe any optical element by a 2x2 transformation matrix $\hat{\mathcal{J}}$. The matrix forms for basic optical components are very intuitive.

For instance, a linear polarizer that completely transmits the s-component and completely absorbs the p-component will be described as

$$\hat{\mathcal{J}}_{LP}^{(s)} = \begin{pmatrix} 1 & 0 \\ 0 & 0 \end{pmatrix}. \tag{2.32}$$

Polarizer with its transmission axis rotated by an arbitrary angle α from the s-axis

$$\begin{aligned} \hat{\mathcal{J}}_{LP}(\alpha) &= \begin{pmatrix} \cos\alpha & -\sin\alpha \\ \sin\alpha & \cos\alpha \end{pmatrix} \begin{pmatrix} 1 & 0 \\ 0 & 0 \end{pmatrix} \begin{pmatrix} \cos\alpha & \sin\alpha \\ -\sin\alpha & \cos\alpha \end{pmatrix} \\ &= \begin{pmatrix} \cos^2\alpha & \sin\alpha\cos\alpha \\ \sin\alpha\cos\alpha & \sin^2\alpha \end{pmatrix}, \end{aligned} \tag{2.33}$$

which corresponds to first rotating $\boldsymbol{J}$ by angle $-\alpha$, polarizing in s and rotating back by α.

Dichroic retarder with its fast axis along s imposing a phase retardation of δ upon the p-polarized light can be written as

$$\hat{\mathcal{J}}_{\lambda} = \begin{pmatrix} 1 & 0 \\ 0 & \mathrm{e}^{\mathrm{i}\delta} \end{pmatrix}. \tag{2.34}$$

Finally, the sample's reflection matrix takes the most general form

$$\mathcal{R} = \begin{pmatrix} r_{ss} & r_{sp} \\ r_{ps} & r_{pp} \end{pmatrix}, \tag{2.35}$$

where

$$r_{ij} \overset{\text{def}}{=} \frac{E_i^{(r)}}{E_j^{(i)}}, \quad i,j \in \{s,p\} \tag{2.36}$$

are complex numbers called *the Fresnel coefficients* and the superscripts $^{(i)}$ and $^{(r)}$ denote the "incident" and "reflected" amplitudes.

So for example r_{sp} tells us what fraction of the incoming p-polarized light will get reflected as s-polarized and how its phase will change. We will examine the Fresnel coefficients in Sec. 2.3.2.

The fact that the off-diagonal components r_{sp} and r_{ps} are generally not zero gives rise to the ellipsometric angles ϵ and θ.

2.2.4. Complex Kerr angle

Although generally not zero, the off-diagonal components of $\mathcal{R}$ are very small, much smaller than the diagonal ones. To illustrate their role, consider an initially s-polarized

plane wave being reflected from a sample that is described by $\mathcal{R}$. Writing this down in the language of Jones formalism

$$\begin{aligned} \boldsymbol{J}^{(i)} &= \begin{pmatrix} 1 \\ 0 \end{pmatrix}, \\ \boldsymbol{J}^{(r)} &= \begin{pmatrix} r_{ss} & r_{sp} \\ r_{ps} & r_{pp} \end{pmatrix} \begin{pmatrix} 1 \\ 0 \end{pmatrix} = r_{ss} \begin{pmatrix} 1 \\ \frac{r_{ps}}{r_{ss}} \end{pmatrix}, \end{aligned} \tag{2.37}$$

where $\frac{r_{ps}}{r_{ss}}$ is a small complex number.

This is the description of an elliptically polarized light just as in (2.28). So in this case, the complex angle Φ is defined by the Fresnel coefficients. We can repeat the same reasoning for *s*-polarized light. This motivates the definition of the *complex Kerr angles* [27, p. 13]

$$\begin{aligned} \Phi_{Ks} &\equiv \theta_{Ks} + \mathrm{i}\epsilon_{Ks} \stackrel{\text{def}}{=} -\frac{r_{ps}}{r_{ss}}, \\ \Phi_{Kp} &\equiv \theta_{Kp} + \mathrm{i}\epsilon_{Kp} \stackrel{\text{def}}{=} \frac{r_{sp}}{r_{pp}}. \end{aligned} \tag{2.38}$$

The subscripts s (p) remind us, that the definition is only meaningful for incident *s*-polarized (*p*-polarized) light.

In the following, we will examine how the Fresnel coefficients r_{ij} change with changing $\boldsymbol{M}$ of the reflective surface.

2.3. Light in anisotropic media

Already Michael Faraday noted that the action of magnetic field on light is not direct. A matter is needed. The external applied magnetic field $\boldsymbol{B}$ changes the magnetization $\boldsymbol{M}$ of a piece of material. The spin-orbit interaction transfers these changes in magnetization to changes of electron motion and light, which interacts with these electrons, will behave differently as a result.

Macroscopically, the interaction of matter with electromagnetic field can be described if the form of the permittivity tensor $\widehat{\varepsilon}$ and the permeability tensor $\hat{\mu}$ are known [9, 26]. In fact, it has been shown that for visible and near-infrared light their frequency is high enough to consider $\hat{\mu}$ as a scalar quantity $\mu_r \approx \mu_0$ [29, 30]. In the following section, we focus on the permittivity tensor $\widehat{\varepsilon}$.

2.3.1. Electric permittivity tensor

If we assume that the effect of magnetization $\boldsymbol{M}$ on $\widehat{\varepsilon}$ is small, we can expand $\widehat{\varepsilon}$ as a function of the magnetization direction $\boldsymbol{m} = (m_x, m_y, m_z)$ [31] - a unitary vector[5] along $\boldsymbol{M}$. Usually, expanding up to 2nd order in $\boldsymbol{m}$ is enough.

For a cubic crystal, which has the highest symmetry of all crystal lattices, the form of $\widehat{\varepsilon}$ is obtained after applying the symmetry arguments [26]

$$\widehat{\varepsilon} = \varepsilon_{xx} \begin{pmatrix} 1 & -iQm_z & iQm_y \\ iQm_z & 1 & -iQm_x \\ -iQm_y & iQm_x & 1 \end{pmatrix} + \begin{pmatrix} B_1 m_x^2 & B_2 m_x m_y & B_2 m_x m_z \\ B_2 m_x m_y & B_1 m_y^2 & B_2 m_y m_z \\ B_2 m_x m_z & B_2 m_y m_z & B_1 m_z^2 \end{pmatrix}, \tag{2.39}$$

[5] it's components are called the *direction cosines* of $\boldsymbol{M}$

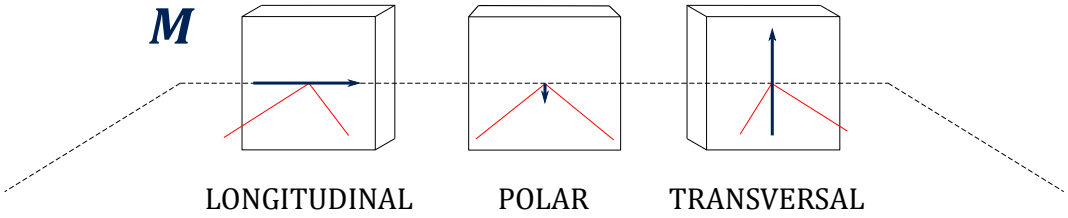

Figure 2.5: The three special cases of magnetization orientation with respect to the light propagation.

where the material constant $Q \in \mathbb{C}$ is called *the Voigt constant*, B_1 and B_2 describe the second-order magneto-optic effect and the coordinate system is as shown in Fig. 2.2.

From the first tensor (linear in $\boldsymbol{m}$), it can be seen that there are 3 special cases for the magneto-optical effect (Fig. 2.5):

- when $\boldsymbol{M}$ lies in the plane of incidence and perpendicular to the sample surface ($m_z = 1\,, m_x = m_y = 0$), the effect is called the *polar MOKE*,
- when $\boldsymbol{M}$ lies in the plane of incidence and along the sample surface ($m_y = 1\,, m_x = = m_z = 0$), the effect is called the *longitudinal MOKE*,
- when $\boldsymbol{M}$ lies perpendicular to the plane of incidence and along the sample surface ($m_x = 1\,, m_y = m_z = 0$), the effect is called the *transversal MOKE*.

Physical models

To derive Eq. (2.39), bare symmetry arguments are applied—the symmetry of the cubic lattice as well as the symmetry of magnetic field. Beyond the symmetry approach, there exists a simple model that results in the same form of $\hat{\varepsilon}$. It is called the *Drude-Lorentz model* [32, p. 191] and it considers the electron as a harmonic oscillator, damped in the material and driven by the oscillating electromagnetic field that light is.

For metals, free electrons dominate the behavior and a typical electron can no more be imagined as an oscillator bound to a nucleus. For this reason, a more rigorous approach based on relativistic quantum mechanics was derived for metals by Petros N. Argyres in 1955 [33] and is called the *Argyres theory*.

Once the form of $\hat{\varepsilon}$ is known, all that's left is to express the Fresnel coefficients in terms of its components. The process, however, is very elaborate. In the next section we outline how it is done.

2.3.2. Wave equation in tensor form

Before approaching the process of reflection, which happens on a boundary between two materials, one needs to inspect how light behaves in each of the materials separately. This is done by solving the wave equation (2.15).

Akin to Višňovský [9], we define the wave-vector $\boldsymbol{k}$ by the complex refractive indices in the particular directions

$$\boldsymbol{k} = \frac{\omega}{c}(N_x, N_y, N_z)\,. \tag{2.40}$$

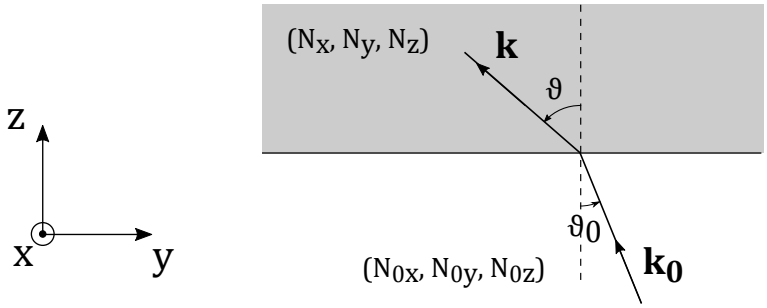

Figure 2.6: Refraction of light from medium characterized by N_0 to a medium with N

To consolidate with the more widely used notation

$$\begin{aligned} N_y &\equiv N \sin\vartheta\,, \\ N_z &\equiv N \cos\vartheta\,, \end{aligned} \tag{2.41}$$

where N is the refractive index and ϑ the angle of incidence.

1. $N_x = 0$ by our choice of coordinate system (Fig. 2.2)—the light does not propagate along x axis.

2. N_y is obtained directly from Snell's law [25, 32]

$$N \sin\theta = N_0 \sin\theta_0\,, \tag{2.42}$$

which is equivalent to

$$N_y = N_{y0}\,. \tag{2.43}$$

3. N_z is calculated from the wave equation (2.15) which reads in a matrix form [9]

$$\begin{pmatrix} N_y^2 + N_z^2 - \varepsilon_{xx} & -N_x N_y - \varepsilon_{xy} & -N_x N_z - \varepsilon_{xz} \\ -N_y N_x - \varepsilon_{yx} & N_x^2 + N_z^2 - \varepsilon_{yy} & -N_y N_z - \varepsilon_{yz} \\ -N_z N_x - \varepsilon_{zx} & -N_z N_y - \varepsilon_{zy} & N_x^2 + N_y^2 - \varepsilon_{zz} \end{pmatrix} \begin{pmatrix} E_x \\ E_y \\ E_z \end{pmatrix} = \boldsymbol{0}\,. \tag{2.44}$$

Equation (2.44) is an *eigenvalue problem* [28, p. 148]. Solving it gives us the *proper modes*—the polarization states that do not change when propagating through the medium. It gives us also refractive indeces N_z for these states. Let us show an example.

Refractive index in an isotropic medium at normal incidence

In an isotropic medium[6], the refractive index in all directions is

$$N = \sqrt{\mu_r \varepsilon_r}\,, \tag{2.45}$$

which comes naturally from the wave equation where permeability and permittivity are considered scalar quantities. To transit to the tensor form, we express $\widehat{\varepsilon}$ as a diagonal

[6] and in cubic crystals as well

tensor with only one component ε_{xx}. This is mathematically equivalent to considering $\widehat{\varepsilon}$ as scalar ε_{xx}. Suppose we let the light propagate along the z axis, which by Fig. 2.2 is the direction perpendicular to the sample surface. When propagating like this, the light is said to be at "normal incidence" and $N_y = 0$. Then Eq. (2.44) becomes

$$\begin{pmatrix} N_z^2 - \varepsilon_{xx} & 0 & 0 \\ 0 & N_z^2 - \varepsilon_{xx} & 0 \\ 0 & 0 & -\varepsilon_{xx} \end{pmatrix} \begin{pmatrix} E_x \\ E_y \\ E_z \end{pmatrix} = \boldsymbol{0}\,. \tag{2.46}$$

As in all eigenvalue problems, this equation has a non-trivial solution if the determinant equals zero. So we have

$$-\varepsilon_{xx}(N_z^2 - \varepsilon_{xx})^2 = 0\,, \tag{2.47}$$

and hence

$$N_z = \pm\sqrt{\varepsilon_{xx}}\,, \tag{2.48}$$

where the minus sign is for the wave propagating in the negative z direction. This is equivalent to Eq. (2.45) (with the notation $\varepsilon_r \equiv \varepsilon_{xx}$ and supposing $\mu_r = 1$ which we have justified by resorting only to the visible light).

Substituting (2.48) back into (2.46), we solve for $\boldsymbol{E}$ getting the 4 proper modes

$$\boldsymbol{E}_{1,2} = \begin{pmatrix} \pm 1 \\ 0 \\ 0 \end{pmatrix}, \quad \boldsymbol{E}_{3,4} = \begin{pmatrix} 0 \\ \pm 1 \\ 0 \end{pmatrix}. \tag{2.49}$$

There is no polarization in z, which is reasonable, since light is a transversal wave and in this case it propagates along z.

Now let us add some *off-diagonal* components to $\widehat{\varepsilon}$.

The polar Kerr effect at normal incidence

The simplest magneto-optical effect is the polar Kerr effect with light at normal incidence, so again $N_x = N_y = 0$. For polar MOKE, we consider $\widehat{\varepsilon}$ to be the linear part of (2.39) with $m_x = m_y = 0$. To get the proper modes and their refractive indices, we solve the equation

$$\begin{pmatrix} N_z^2 - \varepsilon_{xx} & \varepsilon_{xy} & 0 \\ -\varepsilon_{xy} & N_z^2 - \varepsilon_{xx} & 0 \\ 0 & 0 & -\varepsilon_{xx} \end{pmatrix} \begin{pmatrix} E_x \\ E_y \\ E_z \end{pmatrix} = \boldsymbol{0}\,. \tag{2.50}$$

Laying the determinant equal to zero

$$-\varepsilon_{xx}(N_z^4 - 2N_z^2\varepsilon_{xx} + \varepsilon_{xx}^2 + \varepsilon_{xy}^2) = 0 \tag{2.51}$$

and considering only the linear magneto-optic effect by identifying $\frac{\varepsilon_{xy}}{\varepsilon_{xx}} = -iQm_z$, we get

$$\begin{aligned} |N_{z,\pm}| &= \sqrt{\varepsilon_{xx}}\sqrt{1 \pm Qm_z} \\ &\approx \sqrt{\varepsilon_{xx}}(1 \pm \frac{1}{2}Qm_z)\,. \end{aligned} \tag{2.52}$$

The absolute value hides the fact that there are forward-going and backward-going states, just as in the case of isotropic medium above.

Substituting Eq. (2.52) back into (2.50), we get the proper modes

$$\boldsymbol{E}_+ = \begin{pmatrix} 1 \\ -i \\ 0 \end{pmatrix}, \quad \boldsymbol{E}_- = \begin{pmatrix} 1 \\ i \\ 0 \end{pmatrix}, \tag{2.53}$$

which are the right-circular and left-circular polarizations from (2.26).

This is an illustrative result. As described in [8], we can imagine electrons as particles following circular orbits around the nucleus. A magnetic field applied along z will act on these electrons by the Lorentz force (2.13) and decrease the orbit radius of the right-orbiting electrons and increase it for the left-orbiting ones. The polarization $\boldsymbol{P}$ and hence also $\hat{\varepsilon}$ depend on the radius of the circular orbits. So as a result of the perpendicular magnetization, the LCP and RCP light, which drives the electrons, will have a different index of refraction.

Using the derived index of refraction in the well-known Fresnel reflection coefficient for normal incidence

$$r = \frac{1 - N_z}{1 + N_z}, \tag{2.54}$$

it is clear that the two polarization modes will reflect differently.

2.3.3. Boundary conditions

The *boundary conditions* are the four equations that relate the electromagnetic fields $\boldsymbol{E}$, $\boldsymbol{D}$, $\boldsymbol{B}$ and $\boldsymbol{H}$ at one side of a material boundary with the fields $\boldsymbol{E}_1$, $\boldsymbol{D}_1$, $\boldsymbol{B}_1$ and $\boldsymbol{H}_1$ on the other side. By the subscript $\perp$ we denote the vector component perpendicular to the boundary and by $\parallel$ the component parallel to the boundary[7]. The boundary conditions read

$$\begin{aligned} E_{1\parallel} - E_{\parallel} &= 0\,, \\ D_{1\perp} - D_{\perp} &= \sigma_f\,, \\ B_{1\parallel} - B_{\parallel} &= 0\,, \\ H_{1\perp} - H_{\perp} &= K_f\,, \end{aligned} \tag{2.55}$$

where σ_f is a free *surface charge density* and $\mathbf{K_f}$ is the *surface current density*.

Stated in words: the component of $\boldsymbol{E}$ parallel to the boundary and also the component of $\boldsymbol{B}$ perpendicular to the boundary are continuous functions of position, while the perpendicular component of $\boldsymbol{D}$ and the parallel component of $\boldsymbol{H}$ are continuous only if there are no free charges or free currents on the boundary.

The four relations can be derived directly from the Maxwell equations applying them to an infinitesimal region crossing the boundary [23].

[7] by saying "the boundary" we mean the tangential plane to the boundary at the particular point

2.3.4. Fresnel coefficients

The Fresnel coefficients

$$r_{ij} \stackrel{\text{def}}{=} \frac{E_i^{(r)}}{E_j^{(i)}}\,, \quad i,j \in \{s,p\}\,, \tag{2.56}$$

for a general permittivity tensor $\hat{\varepsilon}$ can be calculated by solving the wave equation (2.44) and applying the boundary conditions (2.55). The work was done by Višňovský [9, p. 30–40], for instance.

Explicit formulas for $r_{ij}(\boldsymbol{m})$ when considering only the permittivity components of (2.39) linear in $\boldsymbol{m}$ can be found in [34]:

$$\begin{aligned}
r_{ss} &= \frac{n_0\cos\theta_0 - n\cos\theta}{n_0\cos\theta_0 + n\cos\theta}\,,\\
r_{sp} &= i\frac{n_0 n\cos\theta_0(m_z\cos\theta + m_y\sin\theta)Q}{(n\cos\theta_0 + n_0\cos\theta)(n_0\cos\theta_0 + n\cos\theta)\cos\theta}\,,\\
r_{ps} &= i\frac{n_0 n\cos\theta_0(m_z\cos\theta - m_y\sin\theta)Q}{(n\cos\theta_0 + n_0\cos\theta)(n_0\cos\theta_0 + n\cos\theta)\cos\theta}\,,\\
r_{pp} &= \frac{n\cos\theta_0 - n_0\cos\theta}{n\cos\theta_0 + n_0\cos\theta} - i\frac{2n_0 n\cos\theta_0\sin\theta m_x Q}{n\cos\theta_0 + n_0\cos\theta}\,.
\end{aligned} \tag{2.57}$$

The properties of the reflection matrix are more clear if we rewrite these formulas by defining the complex coefficients α, β and γ, which are functions of n_0, n, θ_0 and Q [35]:

$$\mathcal{R} = \begin{pmatrix} r_{ss} & \alpha m_y + \gamma m_z \\ -\alpha m_y + \gamma m_z & r_{pp} + \beta m_x \end{pmatrix}. \tag{2.58}$$

2.4. Experimental techniques in magneto-optics

There are a few techniques used widely for the study of magneto-optical effects [27]. The simplest one uses just two polarizers, almost perpendicular to each other. The second one, based on a differential intensity detection, uses a Wollaston prism instead of the second polarizer. The prism separates the two polarizations and we can detect intensity from both and compare them. This results in a higher signal-to-noise ratio. An additional improvement in noise reduction is obtained via modulation techniques. Light modulation can be done by a photoelastic modulator based on a quickly oscillating quartz crystal. This is the method used for measurements in this thesis.

2.4.1. Nearly crossed polarizers method

The simplest method to detect the Kerr effect is the nearly crossed polarizers method [8, 27] shown in Fig. 2.7. The light source is a laser.

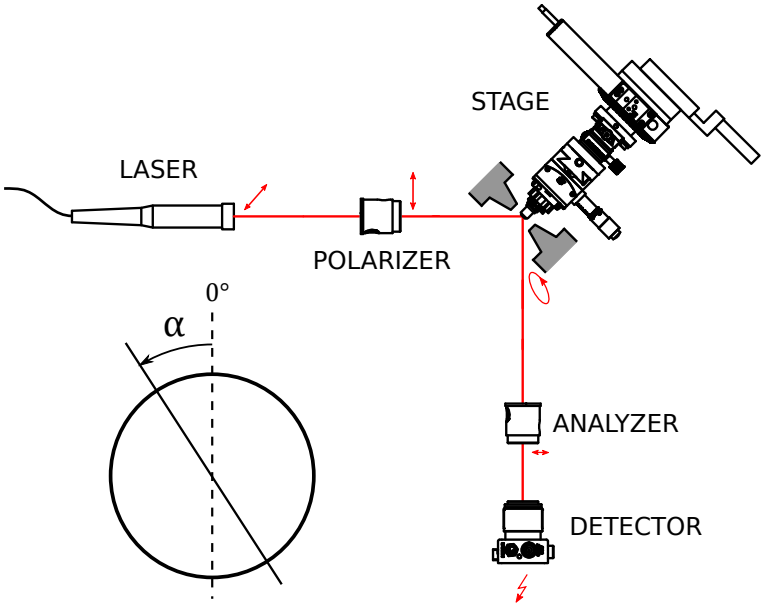

Figure 2.7: A scheme of the nearly crossed polarizers method.

The first polarizing filter called "polarizer" defines the incident light polarization. It's transmission axis is oriented at an angle α counterclockwise from the vertical direction, as shown in Fig. 2.7. The Jones vector after the light passes through the polarizer is then

$$\boldsymbol{J} = \begin{pmatrix} \cos\alpha \\ \sin\alpha \end{pmatrix}. \tag{2.59}$$

After reflection from the magnetized sample, the light becomes elliptically polarized. The second polarizing filter called "analyzer" is set almost 90 degrees from the polarizer. This way we detect only the part of polarization introduced by the Kerr effect, extinguishing (almost) all of the original polarization from the reflected light.

We can calculate the detected light intensity

$$I \propto \boldsymbol{J}^{\dagger}\boldsymbol{J}\,, \tag{2.60}$$

where $\boldsymbol{J}$ is calculated with the help of Jones formalism

$$\begin{pmatrix} J_s \\ J_p \end{pmatrix} = \begin{pmatrix} \cos^2\beta & \sin\beta\cos\beta \\ \sin\beta\cos\beta & \sin^2\beta \end{pmatrix} \begin{pmatrix} r_{ss} & r_{sp} \\ r_{ps} & r_{pp} \end{pmatrix} \begin{pmatrix} \cos\alpha \\ \sin\alpha \end{pmatrix}, \tag{2.61}$$

where α is the orientation of the polarizer and β is the orientation of the analyzer.

Let's look at the special case $\alpha = 0°$ (so that the light incident on the sample is s-polarized). We Taylor expand $\cos\beta$ and $\sin\beta$ at 90° to 1st order so that

$$\begin{aligned}\boldsymbol{J} &= \begin{pmatrix}\cos^2\beta & \sin\beta\cos\beta\\ \sin\beta\cos\beta & \sin^2\beta\end{pmatrix}\begin{pmatrix}r_{ss} & r_{sp}\\ r_{ps} & r_{pp}\end{pmatrix}\begin{pmatrix}1\\0\end{pmatrix}\\ &= r_{ss}\begin{pmatrix}\cos^2\beta & \sin\beta\cos\beta\\ \sin\beta\cos\beta & \sin^2\beta\end{pmatrix}\begin{pmatrix}1\\ \Phi_{Ks}\end{pmatrix}\\ &\approx r_{ss}\begin{pmatrix}0 & -\beta\\ -\beta & 1\end{pmatrix}\begin{pmatrix}1\\ \Phi_{Ks}\end{pmatrix}\\ &= r_{ss}\begin{pmatrix}-\beta\Phi_{Ks}\\ 1-\beta\Phi_{Ks}\end{pmatrix},\end{aligned} \tag{2.62}$$

where we substitute by the complex Kerr angle $\Phi_{Ks} = \theta_{Ks} - i\epsilon_{Ks}$ (2.38).

The light intensity is

$$\begin{aligned}I \propto \left|\begin{pmatrix}-\Delta\beta\Phi_{Ks}\\ 1-\Delta\beta\Phi_{Ks}\end{pmatrix}\right|^2 &= (-\Delta\beta\theta_{Ks})^2 + (-\Delta\beta\epsilon_{Ks})^2 + (1-\Delta\beta\theta_{Ks})^2 + (-\Delta\beta\epsilon_{Ks})^2\\ &\approx 1 - 2\Delta\beta\theta_{Ks}\,,\end{aligned} \tag{2.63}$$

where we neglect the second order terms in θ_{Ks} and ϵ_{Ks}. If β was exactly equal to 90°, no first order terms in θ and ϵ would appear—the little offset $\Delta\beta$ is important.

This setup allows us to measure only the real part of Φ_{Kp}, the kerr rotation θ_K. To measure ϵ_K, we would need to put a QWP between the analyzer and the sample [27, p. 18].

2.4.2. Polarization modulation method

On the setup in Fig. 2.8, three components were added. The quaterwave plate transforms the linear light coming out from the laser into circular. This makes the intensity of light after passing the polarizer independent of the polarizer orientation. A photoelastic modulator (PEM) is a dichroic retarder (2.34) with a harmonically changing phase retardation $\delta = \delta_0\cos(\omega t)$ [26, p. 62]. Including it into the set-up will give us 2 main advantages.

The first advantage is the high signal to noise ratio. The voltage detected is passed to a *lock-in amplifier*, which picks out only the frequency at which the PEM oscillates (50 kHz in our case), thus leaving only the desired signal and getting rid of the noise.

The second advantage is the capability of measuring both the real and imaginary parts of Φ_{Ks} at the same time [10]. This can be shown using the Jones formalism.

Modifying (2.62) by introducing a phase retarder (2.34), we have

$$\boldsymbol{J} = r_{ss}\begin{pmatrix}\cos^2\beta & \sin\beta\cos\beta\\ \sin\beta\cos\beta & \sin^2\beta\end{pmatrix}\begin{pmatrix}1 & 0\\ 0 & \mathrm{e}^{i\delta_0\cos(\omega t)}\end{pmatrix}\begin{pmatrix}1\\ \Phi_{Ks}\end{pmatrix}. \tag{2.64}$$

We next use the Jacobi-Anger expansion up to second harmonic in ω

$$\mathrm{e}^{i\delta_0\cos(\omega t)} = J_0(\delta_0) + i2J_1(\delta_0)\cos(\omega t) - 2J_2(\delta_0)\cos(2\omega t) + \dots\,, \tag{2.65}$$

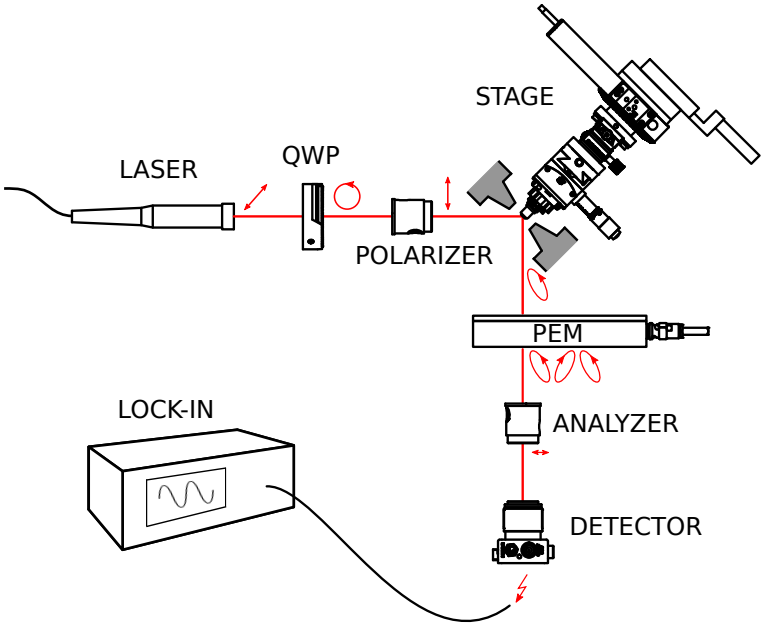

Figure 2.8: A scheme of the polarization modulation method.

where $J_i(\delta_0)$, $i \in \{0, 1, 2\}$ are Bessel functions of the first kind.

This gives us

$$I \propto I_{DC} + I_\omega \cos(\omega t) + I_{2\omega} \cos(2\omega t)\,, \tag{2.66}$$

where

$$I_{DC} = \cos^2 \alpha + \sin(2\alpha) J_0(\delta_0) \theta_{Ks} \tag{2.67a}$$
$$I_\omega = -2J_1(\delta_0) \sin(2\alpha) \epsilon_{Ks} \tag{2.67b}$$
$$I_{2\omega} = -2J_2(\delta_0) \sin(2\alpha) \theta_{Ks}\,. \tag{2.67c}$$

I_{DC} can be further simplified by choosing the modulation amplitude $\delta_0 \doteq 2,404$ so that $J_0(\delta_0) = 0$.

By measuring the DC voltage as well as the amplitudes of the voltage oscillating at ω and 2ω (using a lock-in amplifier), one can get the ellipsometric angles quantitatively

$$\theta_{Ks} = -\frac{I_{2\omega}}{I_{DC}} \frac{\operatorname{cotg} \alpha}{4J_2(\delta_0)}\,, \tag{2.68a}$$
$$\epsilon_{Ks} = -\frac{I_\omega}{I_{DC}} \frac{\operatorname{cotg} \alpha}{4J_1(\delta_0)}\,, \tag{2.68b}$$

where $\operatorname{cotg} \alpha$, $J_1(\delta_0)$ and $J_2(\delta_0)$ stay constant during a measurement.

3. Optical setup and calibration procedure

This chapter introduces the optical setup, the control software and the calibration procedure for determining the plane of incidence.

3.1. Optical setup

There are several ways to build a functional ellipsometric setup using a photoelastic modulator. Polisetty et al. [36] investigated them in detail and compared their capabilities. In this work we are using the configuration with the highest signal to noise ratio, which also has the ability to measure both harmonics, I_ω and $I_{2\omega}$ with comparable sensitivity.

The 3D model of the set-up is in Fig. 3.2. The detailed view of the rotation stage is in Fig. 3.3. The angle of incidence of the light on the sample is set to be 45 °, which is convenient for optical components alignment and it usually gives good ellipsometric angles amplitudes - Fig. 3.1.

The light source is an ultra low-noise laser diode module provided by Coherent, Inc., emitting a 635 nm light with a power of 5 mW. The Glan-Taylor polarizing filters GT10-A by Thorlabs, Inc. have an extinction ratio of 100 000:1. Their stepper motor rotating stages are the K10CR1 with an absolute accuracy of $\pm 0,14$ °. We use the photoelastic modulator PEM-100 by Hinds Instruments oscillating at the nominal frequency of 50 kHz, providing a TTL signal at the oscillating frequency as a reference to the AMETEK 7270 digital lock-in amplifier. The lock-in amplifier is further connected to the PDA36A Si amplified photodetector. The temperature controller, Thorlabs TED200C, uses a PID to control and stabilize the temperature of the Peltier heater. In a stabilized state, the temperature oscillates at worst with a peak-to-peak amplitude of $\sim$ 0,2 °C.

Most of the components used here were used before in a very similar setup based on the Generalized Magneto-optical Ellipsometry (GME) method [38, 39]. The GME setup was designed by Ing. Lukáš Flajšman and built, programmed and modified by Bc. Ondřej Wojewoda. My input into the construction was designing a new heat sink for the Peltier and, with the help of Lukáš Flajšman, also a few other components for being able to add a second 2D translation stage. These changes to the setup were necessary for automation of the magnetic anisotropy measurements described in Chapter 4.

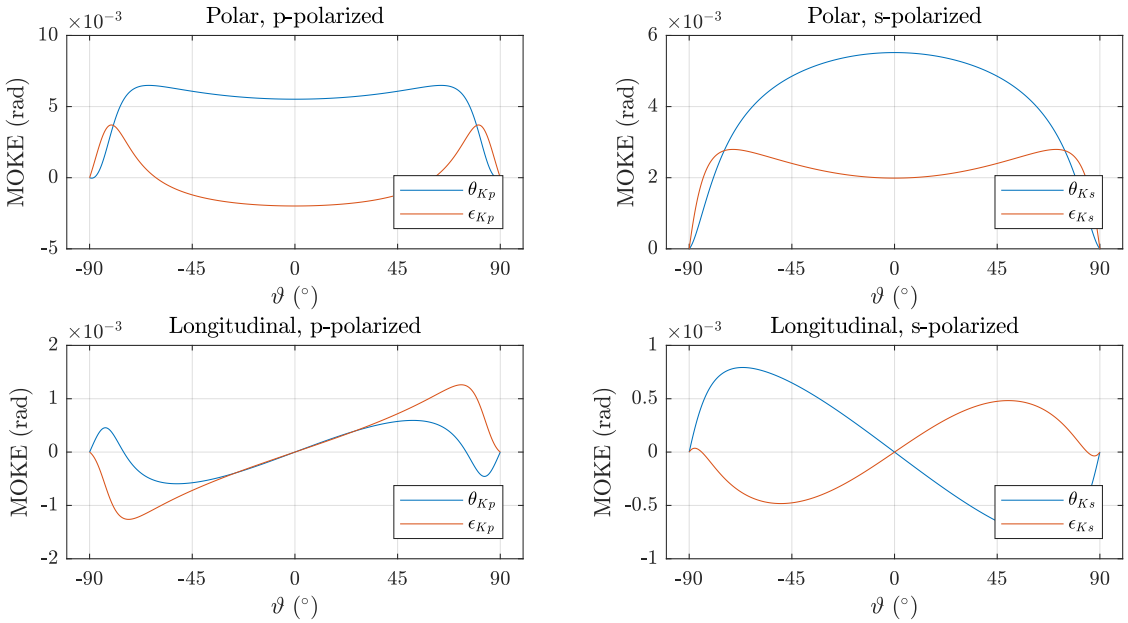

Figure 3.1: Dependence of the Kerr ellipticity ϵ_{Ks} and ϵ_{Kp} and Kerr rotation θ_{Ks} and θ_{Kp} (2.38) on the angle of incidence, as calculated from (2.57) using the definition in (2.38). The complex index of refraction for Co $n_{Co} = 2,2157 + i4,1786$ can be found on `www.refractiveindex.info` and the Voigt constant $Q_{Co} = 0,0283 - i0,003$ was measured by Arregi et al. [37].

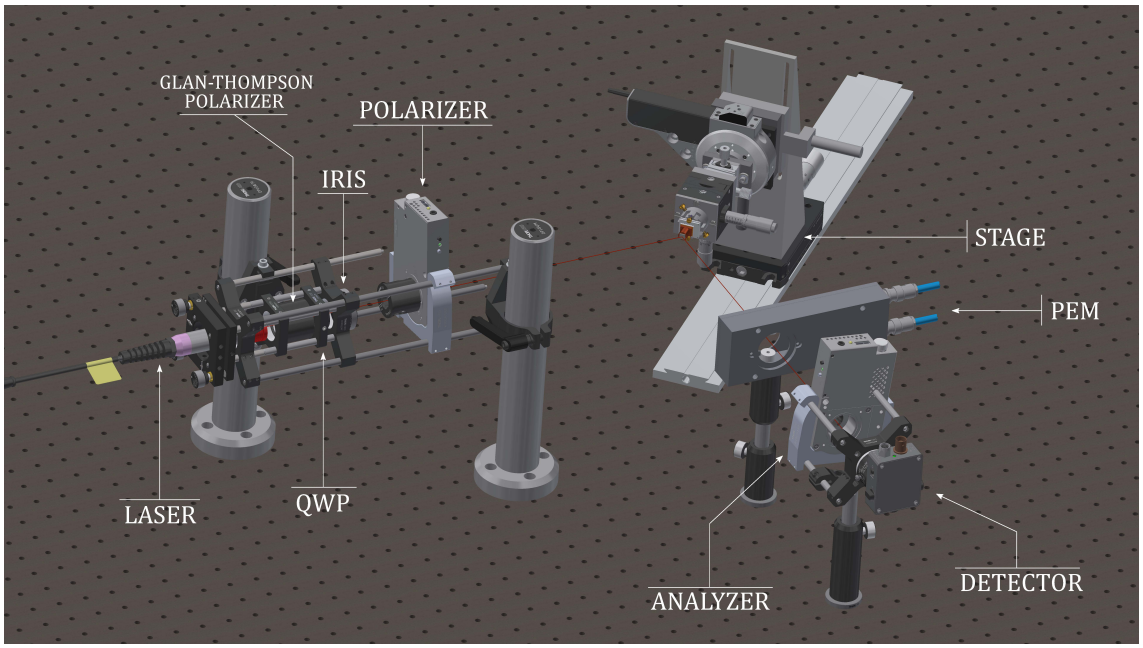

Figure 3.2: 3D model of the ellipsometric setup. The light passes through a Glan-Thompson polarizer and gets circularly polarized at the quaterwave plate. That insures the same incident intensity for any direction of the polarizer. After being linearly polarized (in s-direction) on the polarizer and elliptically polarized after reflection from the sample, the light phase gets modulated at PEM. The analyzer is the last linear polarizer. The light then passes through a red filter and is detected and amplified on the photodetector. An electromagnet, not shown here, applies external magnetic field in plane of the sample, parallel to the optical table surface.

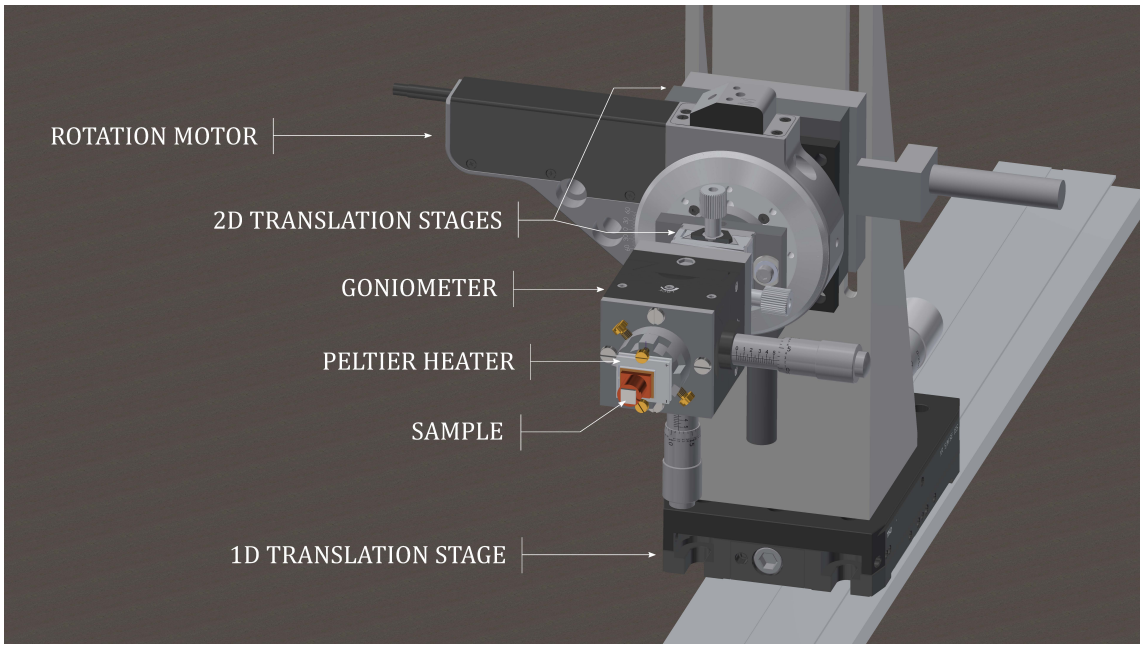

Figure 3.3: The rotational stage in a detailed view. The whole setup can be moved back and forth along an optical rail with a fine movement possible by a microscrew of a 1D translation stage. Movement in the 2 orthogonal axes is possible by 2 separate 2D translation stages, one set behind and one before the rotational motor. Tilt in the2 axes is manually controlled by a goniometer. The Peltier heater with a 10 kΩ thermistor provides a temperature control. An electromagnet, not shown here, applies external magnetic field in plane of the sample, parallel to the optical table surface.

3.2. Control software

The other main task was to enable the automation of the calibration process, measurements and data acquisition. Major part of the work was therefore programming such a control software. It was done in the LabVIEW 2018 development environment which has a native support for creating a Graphical User Interface (Fig. 3.4).

Some of the subroutines used in the software were programmed and kindly provided by Ondřej Wojewoda. These include the polarizer, analyzer and stage stepper motor motion control. Other subroutines, especially the ones for the lock-in amplifier data acquisition, were supplied by the hardware provider himself (AMETEK, Inc.).

The software enables the user to communicate with all the peripherals and to take automatic measurements of hysteresis loops. We can control the sample orientation with respect to the external magnetic field and set the temperature of the sample in the range from 10 °C to 120 °C. The temperature control is important for investigation of the FeRh alloy as shown in Chapter 4. The software also performs the calibration procedure explained in the next section.

3.3. Calibration procedure

It is important to have a well defined plane of incidence. This is because the *s*- and *p*-polarizations are defined by it and the Kerr effect for *s* and *p* is different (Eq. (2.58)). We can find out the *s*-polarization orientation by an indirect ellipsometric method, performing

a simple experiment using the setup in Fig. 2.7. After passing the laser light through a linear polarizer, there is a reflection on the sample and after going through the analyzer, the beam is detected. Assuming that the reflection matrix (2.35) does not contain any off-diagonal elements, this experiment can be described using the Jones formalism

$$J_f = \begin{pmatrix} \cos^2\alpha & \sin\alpha\cos\alpha \\ \sin\alpha\cos\alpha & \sin^2\alpha \end{pmatrix} \begin{pmatrix} r_{ss} & 0 \\ 0 & r_{pp} \end{pmatrix} \begin{pmatrix} \cos^2\beta & \sin\beta\cos\beta \\ \sin\beta\cos\beta & \sin^2\beta \end{pmatrix} \begin{pmatrix} a \\ b \end{pmatrix} \tag{3.1}$$

$$\begin{aligned} I \propto |J_f|^2 = \cos^2\alpha \sin^2\beta \Big[\sin^2\alpha \sin^2\beta + 2 \cdot \mathrm{Re}\left\{\frac{r_{ss}}{r_{pp}}\right\} \sin\alpha\cos\alpha\sin\beta\cos\beta \\ + \left|\frac{r_{ss}}{r_{pp}}\right| \cos^2\alpha\cos^2\beta \Big] . \end{aligned} \tag{3.2}$$

Based on this calculation, the strategy now is to measure the light intensity for a large set of polarizer-analyzer values and fit the measurement by a function

$$\begin{aligned} I = A\Big[\sin^2(\alpha-\alpha_0)\sin^2(\beta-\beta_0) + 2R_1 \sin(\alpha-\alpha_0)\cos(\alpha-\alpha_0)\cdot \\ \cdot \sin(\beta-\beta_0)\cos(\beta-\beta_0) + R_2\cos^2(\alpha-\alpha_0)\cos^2(\beta-\beta_0) + C\Big] . \end{aligned} \tag{3.3}$$

A is the signal amplitude and it is determined by the laser intensity and the photodetector gain. C is the intensity induced by the ambient light and also the *dark current*[1]. The $R_1 \stackrel{\text{def}}{=} \mathrm{Re}\left\{\frac{r_{ss}}{r_{pp}}\right\}$ and $R_2 \stackrel{\text{def}}{=} \left|\frac{r_{ss}}{r_{pp}}\right|$. Most importantly, we add an angular offset term - α_0 (β_0) denote the polarizer (analyzer) angular offset from the s-polarization axis - Fig. 3.4.

By finding α_0 and β_0 we have determined the *s*- and *p*-polarization and therefore the plane of incidence. Moreover, from the R_1 and R_2 parameters we can obtain the complex index of refraction.

[1]The dark current represents the electrons that get excited on a CCD chip by thermal excitations, besides the photon-excited ones.

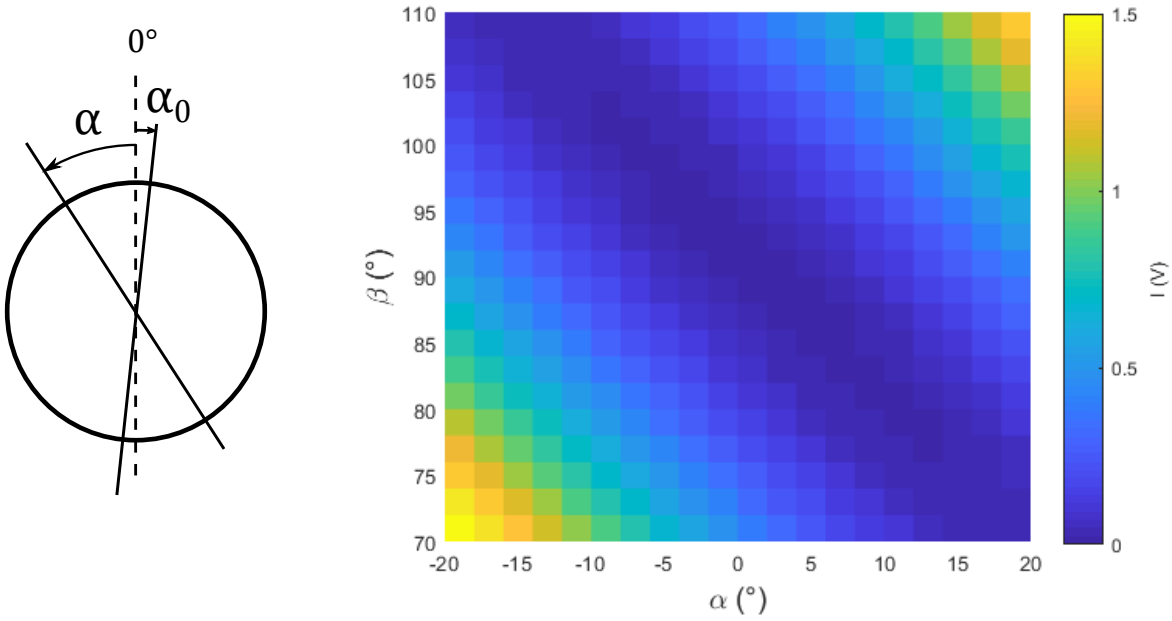

Figure 3.4: Light intensity detected by the photodetector when measuring with the setup in Fig. 2.7 for different analyzer and polarizer angle orientations. This data is fitted for the 6 parameters stated in formula (3.3). α_0 is the angular offset of the polarizer to the s-polarization. With the calibration procedure we try to reach $\alpha_0 = 0°$.

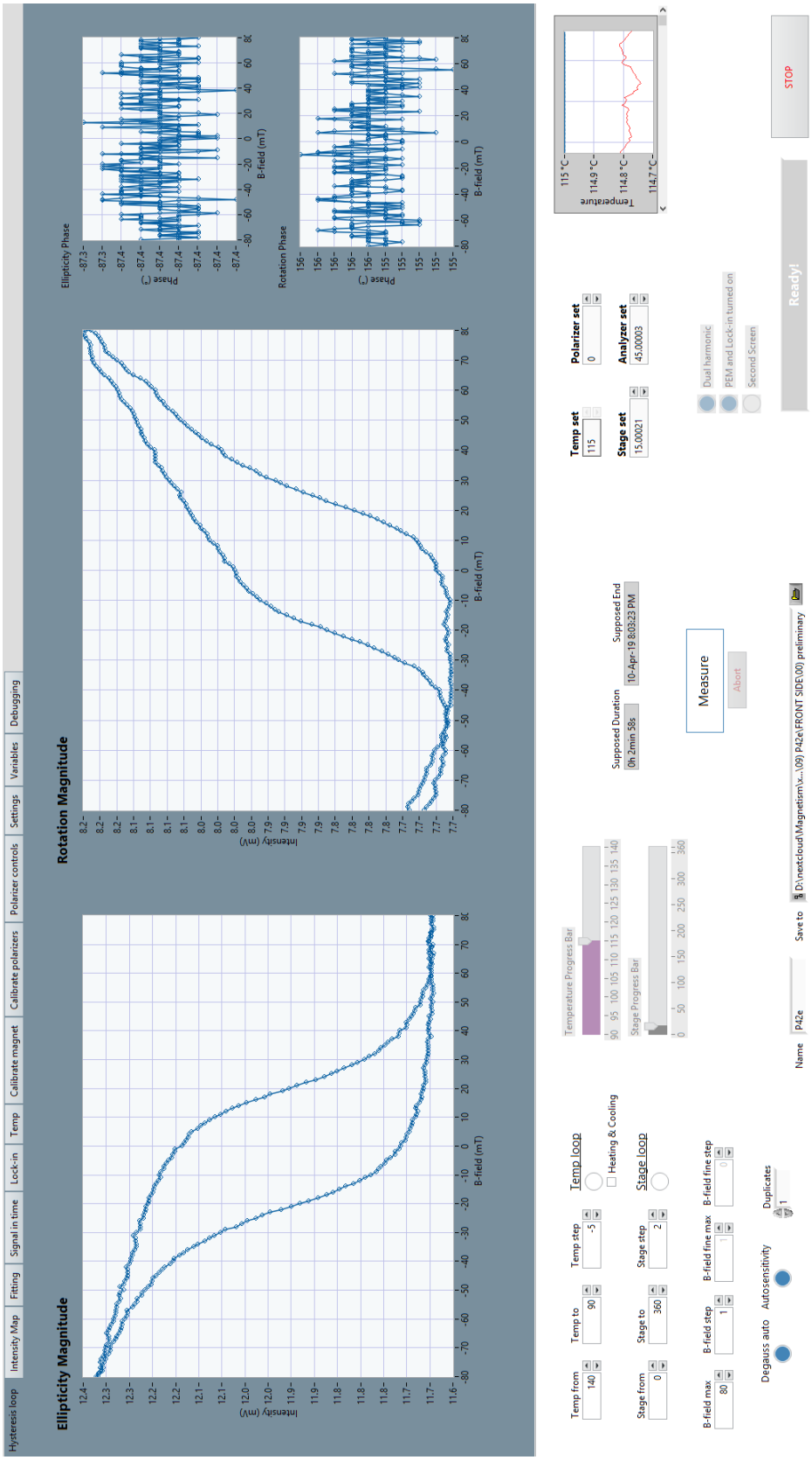

Figure 3.5: The Graphical User Interface of the control software. The main page serves for measuring hysteresis loops at different temperatures and stage rotation angles. Displayed in plots are the Kerr ellipticity and rotation magnitude (hysteresis curve) and phase of the signal with respect to the voltage that drives the PEM. On the right, the temperature reading from a thermistor is plotted in time. Data get saved automatically in the form of a txt file after taking a hysteresis loop.

4. Measurements

A measurement consists of taking hysteresis loops at different temperatures and/or sample orientations. Each hysteresis loop is measured by sweeping the magnetic field from the low negative values to the positive maximum and back. In this process, the first and second harmonic intensity amplitudes I_ω and $I_{2\omega}$ (obtained from the lock-in amplifier), as well as the actual temperature are measured and saved. The first harmonic signal I_ω, proportional to ellipticity, has proven to give a better signal-to-noise ratio than $I_{2\omega}$. Therefore, in all the following measurements, we use exclusively I_ω to interpret the magnetic properties of test samples. It is also I_ω what we refer to as "the magneto-optical signal".

4.1. Epitaxial hcp cobalt film

The first sample measured is a 15-nm-thick layer of hcp cobalt with a strong in-plane[1] uniaxial anisotropy [37]. The sample was prepared via magnetron sputtering by M.Sc. Jon A. Arregi and its composition is depicted in Fig. 4.1 b). The stage with the sample was rotated from 0 ° to 360 ° by 2 ° steps. The measurement was taken at laboratory temperature of 24 °C. The field was swept at a rate of 10 mT/s with 1 mT steps from -80 mT to 80 mT and back.

We can consider the thin film as an infinite plane: an ellipsoid object, suitable to be described by the Stoner-Wohlfarth model. Fitting the hysteresis loops considering the anisotropy energy of Eq. (1.6) turned out to be insufficient. Therefore, two more uniaxial terms have been added to the anisotropy energy

$$E_A = K_u \sin^2 \vartheta + K_{u2} \sin^4 \vartheta + K_{u3} \sin^6 \vartheta \,, \tag{4.1}$$

where both K_{u2} and K_{u3} are anisotropy constants in the units of energy density J·m^{-3}. Beside the three anisotropy coefficients, there are two more degrees of freedom in the fitting. The first one is an angular offset α_0 that is subtracted from the field orientation angle α, to account for the fact, that the EA of our sample does not have to lie along the applied field direction at the beginning of the measurement. The second coefficient is a prefactor coefficient C to multiply all the theoretical $M_\parallel/M_s$ values obtained from the SW model. This prefactor is added because the model provides the value $M_\parallel/M_s \in \{-1, 1\}$, while the measured signal is in the units of mV. Although we divide all the collected data by the highest absolute value measured (which makes all the measured values to lie in the interval $\{-1, 1\}$), this normalization will be affected by an experimental error.

The best fit was obtained for the coefficient values stated in Table 4.1. The energy profile in polar coordinates is drawn in Fig. 4.1 a), the measured and fitted hysteresis

[1] *lying in the plane of the sample*

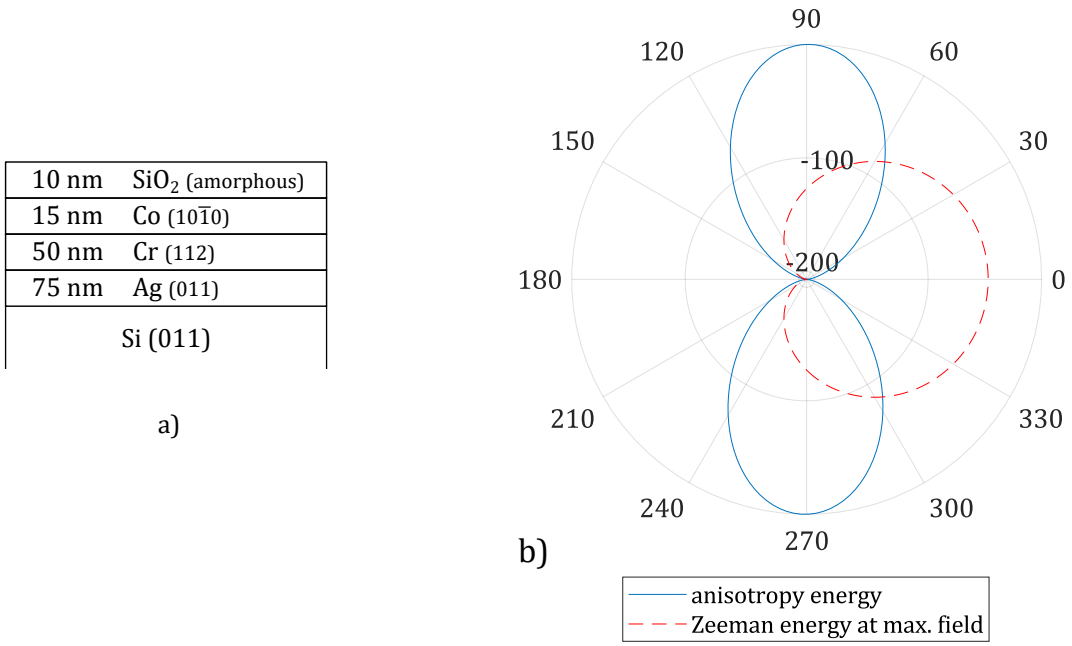

Figure 4.1: a) The sample composition to ensure the strong in-plane uniaxial anisotropy. b) Anisotropy energy profile and compared with the Zeeman energy profile for the field at its highest negative maximum along 0 ° direction. You can see the two are comparable in magnitude, although, as seen when looking at the loops in Fig. 4.2, the maximum field wasn't able to bring the magnetization into saturation at all directions.

loops are in Fig. 4.2 and the measured and theoretical remanence and coercive field are in Fig. 4.3. Note the large coercive field predicted by the model compared to the measured data. This is called *the Brown's paradox* [12]. For the field applied in the EA direction, the coercive field predicted (for the uniaxial E_A from Eq. (1.6)) is $\mu_0 H_A = 2K_u/M_s$, but the coercive field observed may be more than an order of magnitude lower [40]. This discrepancy between the theory and experiment arises because the SW model considers no thermal energy fluctuations, which help overcome the metastable energy barrier, nor does it account for the material defects, which act as nucleation centers for domain wall creation and subsequent propagation. Both, the temperature and the defects, therefore accelerate the magnetization switching process, bringing $\mu_0 H_c$ to lower values. Moreover, the SW model describes correctly only the coherent rotation part of the magnetization reversal which is usually present only at higher applied field values. For these reasons, only the first quarters of the loops are fitted, which is clear from the colormaps in Fig. 4.2.

Table 4.1: The fitted coefficients for the uniaxial hcp cobalt measurement, taking into account the anisotropy energy form (4.1).

$\mu_0 H_u$ (mT)	$\mu_0 H_{u2}$ (mT)	$\mu_0 H_{u3}$ (mT)	α_0 (°)	C
-316.46	142.91	-33.52	89.49	0.9375

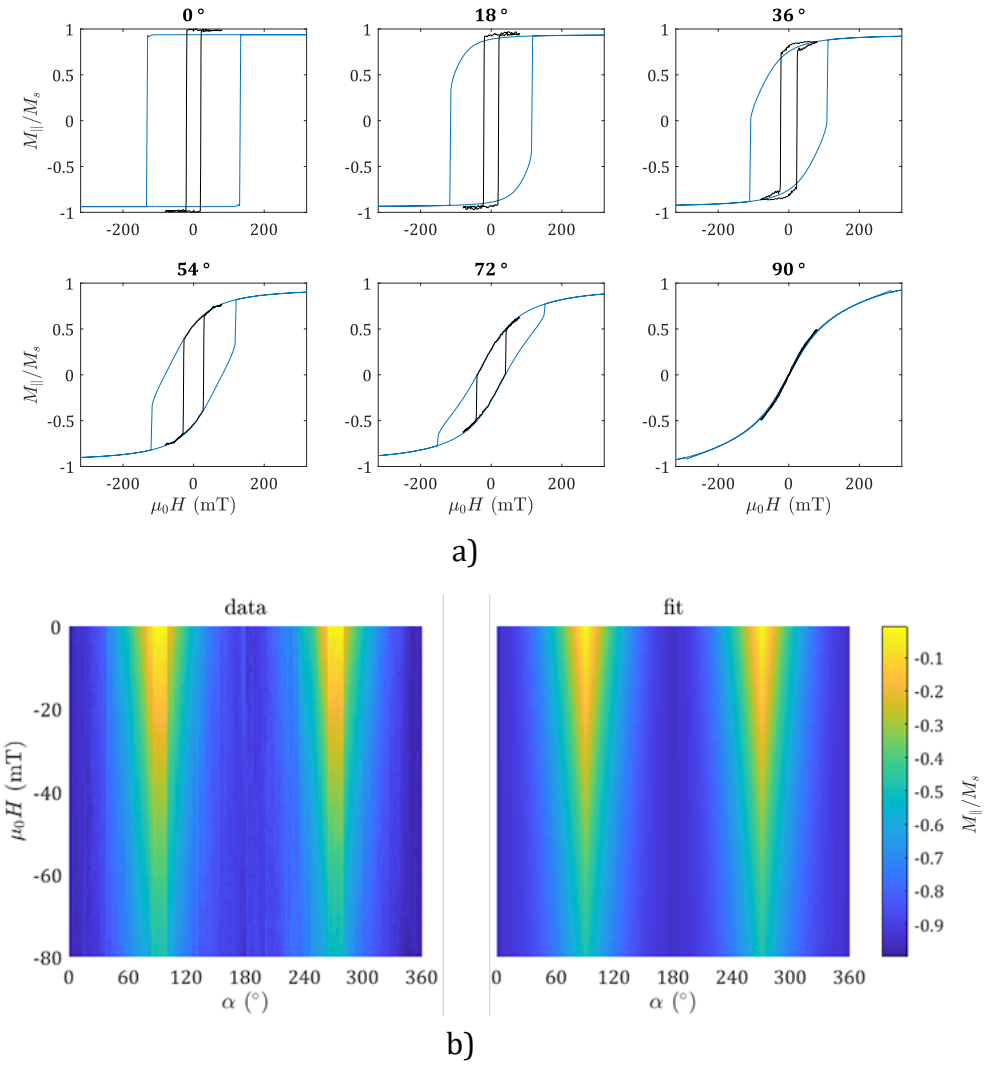

Figure 4.2: a) Hysteresis loops for few selected field orientations including the measurement nearest to the easy axis (0 °) and the hard axis (90 °). b) The first quarter of all loops layed out in a colormap along with the loops fitted by SW model.

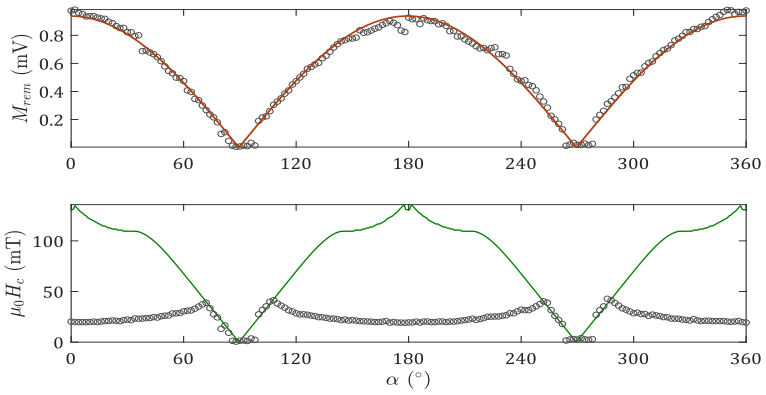

Figure 4.3: The remanent magnetization and coercive field measured and fitted by the SW model with coefficients from Tab. 4.1. The extremely high predicted coercivity values are due to the Brown's paradox.

4.2. Epitaxial FeRh films

The second material examined is the FeRh alloy, with a bcc (CsCl type) lattice and cubic magnetocrystalline anisotropy. The FeRh at almost equiatomic composition undergoes a first-order temperature-driven phase transition from the antiferromagnetic (AF) to the ferromagnetic (FM) phase [41, 42]. This means that after raising the temperature above approximately 60 °C, the ferromagnetic domains start growing in the AF matrix [43, 44]. The AF phase has no net magnetization, so it does not contribute to the magneto-optical signal. We can therefore distinguish the phase transition by plotting the Kerr ellipticity magnitude at the highest applied field against the sample temperature. The temperature is controlled by the Peltier heater, as described in Sec. 3.1.

4.2.1. Phase transition and magnetic anisotropy in FeRh

We illustrate the behaviour of FeRh on a 26 nm thin epitaxial layer grown by the magnetron sputtering on MgO(001) substrate and annealed at 750 °C for 30 minutes (Fig. 4.4). An anisotropy measurement was also performed, with the sample rotated from 0 ° to 360 ° by 2 ° (with $\alpha = 0°$ corresponding to the field oriented along FeRh[110] orientation). The remanent magnetization shows a fourfold anisotropy, typical for cubic crystals, but the two easy axes are not equivalent, as obvious from Fig. 4.5. This could suggest that in this particular sample, there could be a combination of the cubic and uniaxial anisotropy, not necessarily with their easy axes aligned. [14] (The uniaxial energy contribution might occur due to stepped terraces, observed on the surface of the MgO substrate prior to FeRh deposition.) However, a simple sum of these two contributions did not prove to be sufficient to replicate the experimental data. A different approach will be needed.

Both the magnetization and coercive field show a hysteretic temperature dependence. The coercivity is lowest at the high temperature and increases gradually upon cooling, coincident with the appearance of the AF phase (Fig. 4.4). This change in coercivity can be explained by two factors. Firstly, at the lower temperatures, the ferromagnetic phase is no more a uniform film, but rather seggregated domains, surrounded by an AF matrix [43]. While a thin magnetic film will have an in-plane anisotropy to minimize the demagnetizing energy, the isolated FM islands may tend to lie slightly out-of-plane [44], making it harder to orient them along the in-plane applied field. Secondly, the AF inclusions can act as pinning centers for the domain wall, slowing down the magnetization reversal process and increasing H_c. Note that in Fig. 4.4 and all the following figures, the H_c values for lower temperatures are not plotted because the H_c at the low temperature cannot be deduced from the hysteresis loops, as can be seen for instance from the 60 °C loop in Fig. 4.4.

A closer look at the hysteresis loops taken with the field applied close to the hard axis reveals a strange increase in the signal, which emerges when decreasing the field to zero value both from the positive and negative saturation (Fig. 4.6). This could be a manifestation of an unusually big *quadratic magneto-optical effect* seen for instance in a Co_2FeSi Heusler compound [45]. The explanation of why the quadratic MOKE appears is given by the second order electric permittivity tensor from Eq. (2.39), particularly the $m_x m_y$ term. The m_z, for a thin film with in-plane anisotropy, can be considered as constant 0. The magnetization cosine m_x lies always in the applied field direction; it is this component we mostly control. The magnetization cosine m_y lies perpendicular to the applied field,

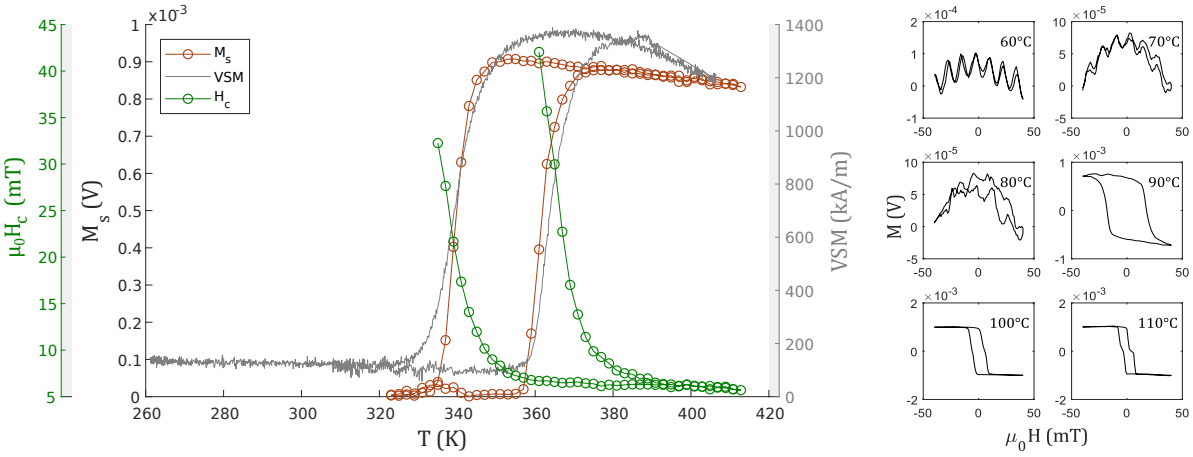

Figure 4.4: The temperature dependance of M_s and H_c measured with MOKE with the field applied at 30 ° from the FeRh [100] direction. For comparison, a vibrating sample magnetometry measurement (VSM) is plotted (credit: Jan Hajduček). On the right side, a few exemplary loops measured upon heating. The oscillations at low temperature measurements are caused by the temperature oscillations and the parabolic shape of these loops might be due to an action of the magnetic field on the mechanical motion of the sample holder.

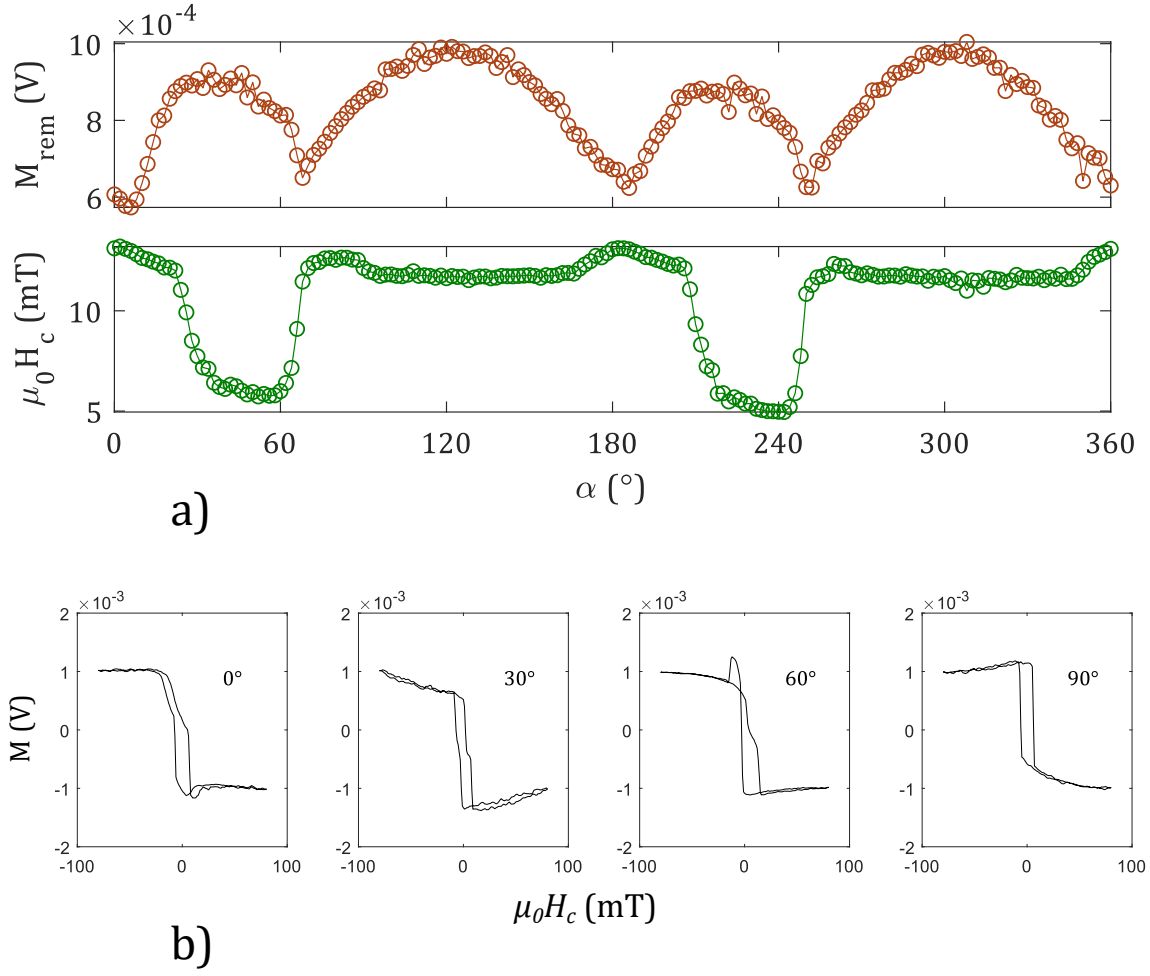

Figure 4.5: a) A fourfold anisotropy with inequivalent anisotropy axes. Measured on a 26 nm FeRh layer on MgO(001) substrate. b) A few exemplary loops obtained in a).

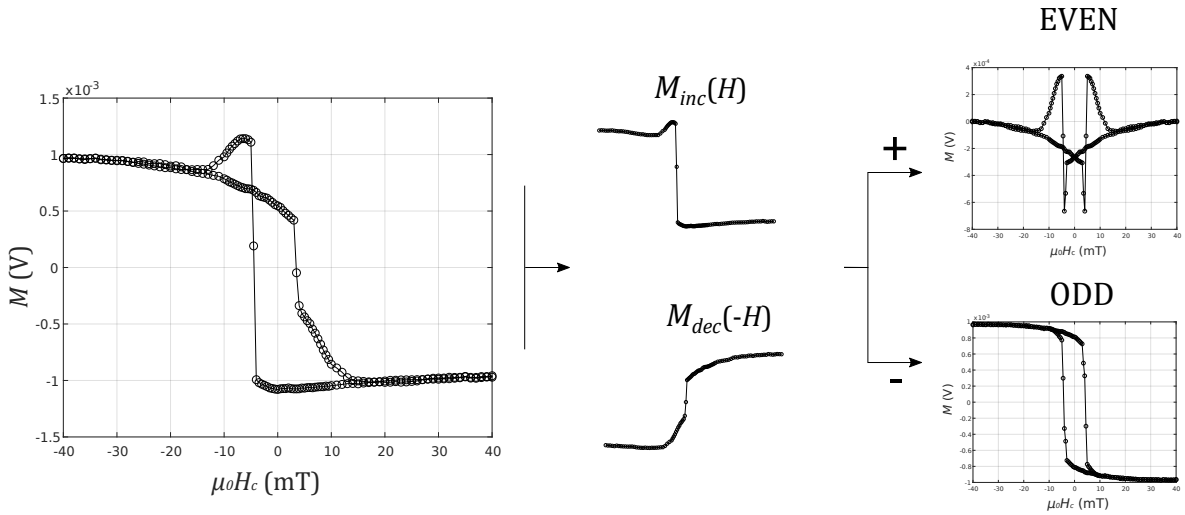

Figure 4.6: The procedure described by Eq. (4.2a) and (4.2b) to isolate the linear and quadratic MOKE contributions.

so at a high enough external field it should be zero, along with the product $m_x m_y$ and no quadratic effect should be observed. But if the applied field is small, the SW model predicts that m_y increases as $\boldsymbol{m}$ coherently rotates. To further support the argument: applying the field along easy axis should not result in the effect, as there will be a sudden switch in the magnetization rather than a gradual rotation of the magnetization vector. This is indeed what we observe in the measurements.

Because the second-order effect seems to happen in the same manner for both the increasing and decreasing field branch of the hysteresis loop[2], we can isolate it from the linear magneto-optic response by subtracting and adding the two branches. If we denote M_{inc} and M_{dec} the hysteresis loop branches where the field increases and decreases respectively, we can calculate two sets of data that we call the *even* and *odd* magnetization as

$$M_{odd}(H) = \Big(M_{inc}(H) - M_{dec}(-H)\Big)/\,2\,, \tag{4.2a}$$

$$M_{even}(H) = \Big(M_{inc}(H) + M_{dec}(-H)\Big)/\,2 \tag{4.2b}$$

Note that by this procedure we get only a half of the data points of the original set $M(H)$. For the plots to be more illustrative, we artificially display complete hysteresis loops by plotting $-M_{odd}(-H)$ along with $M_{odd}(H)$ and $M_{even}(-H)$ along with $M_{even}(H)$. This whole procedure is depicted in Fig. 4.6.

4.2.2. FeRh films on different substrates

The effect of the substrate on the FeRh magnetic properties was investigated. Three samples with FeRh layers of similar thickness on different substrates were measured. The first one is a 40 nm thick layer of FeRh grown on un-annealed MgO(001). Plotting the saturation signal against temperature shows a phase transition, which is also confirmed by a vibrating sample magnetometry measurement (Fig. 4.7 a). While M_s is increasing with temperature, the coercivity decreases, just as in the case of the 26 nm layer from

[2]i.e. the first and second half of the hysteresis loop measurement

Fig. 4.4. Measuring the field direction dependance shows a fourfold anisotropy, which persists when decreasing temperature, but disappears at around 60 °C (Fig. 4.7 b). In the case of the MgO substrate, the lattice parameters of MgO an FeRh match in the way as to let the FeRh grow diagonally to the MgO lattice (Fig. 4.7 c). The lattices do not match precisely, the MgO substrate exerts an in-plane compressive strain on the FeRh lattice and as a result, there is a tetragonal distortion, which makes the FeRh lattice expand slightly in the out-of-plane direction.

The second sample has an additional thin W(001) buffer layer on the MgO(001) substrate. The tungsten layer has a larger lattice parameter, making the FeRh lattice expand in-plane. Despite the opposite effect of the matching lattices—in-plane expansion instead of in-plane constriction—the magnetic behavior seems very similar (Fig. 4.8).

The third thin layer was grown on a saphire Al_2O_3(000 1) which makes the FeRh orient in the (111) direction and the distortion in this case is rhombohedral. Although the AF to FM transition is observed, there is no apparent in-plane magnetic anisotropy in the entire investigated temperature region (Fig. 4.9).

4.2.3. FeRh/MgO interface

The VSM data from all the previous measurements show a non-zero magnetic moment also at the low-temperature state. This would indicate the presence of a remanent FM phase. With the MOKE, which is usually sensitive only to a few tens of nanometers of the measured sample's surface, the signal drops to zero. It is therefore possible, that most of the FM phase at low temperature lie at the boundary with the substrate [46].

Following this argument, we prepared a new sample on a double-polished MgO substrate, which will allow us to measure with the laser light from the back, i.e. from the non-deposited side of the sample without the light being depolarized on the usually rough back side of the substrate. The measurement performed on both the back and the front side is plotted in Fig. 4.10. Indeed, the magnitude of the magneto-optical signal taken at the magnetization saturation, when measured from the back side shows a small but noticeable non-zero value at the low temperatures, which is not present in the front-side measurement.

There are sudden drops in remanence seen in the anisotropy measurement from Fig. 4.10 when measuring from the back side with field applied near the hard axis (90 °, 180 ° etc.). They could be connected with the second-order magneto-optical effect, which shows a change of sign at the same angles.

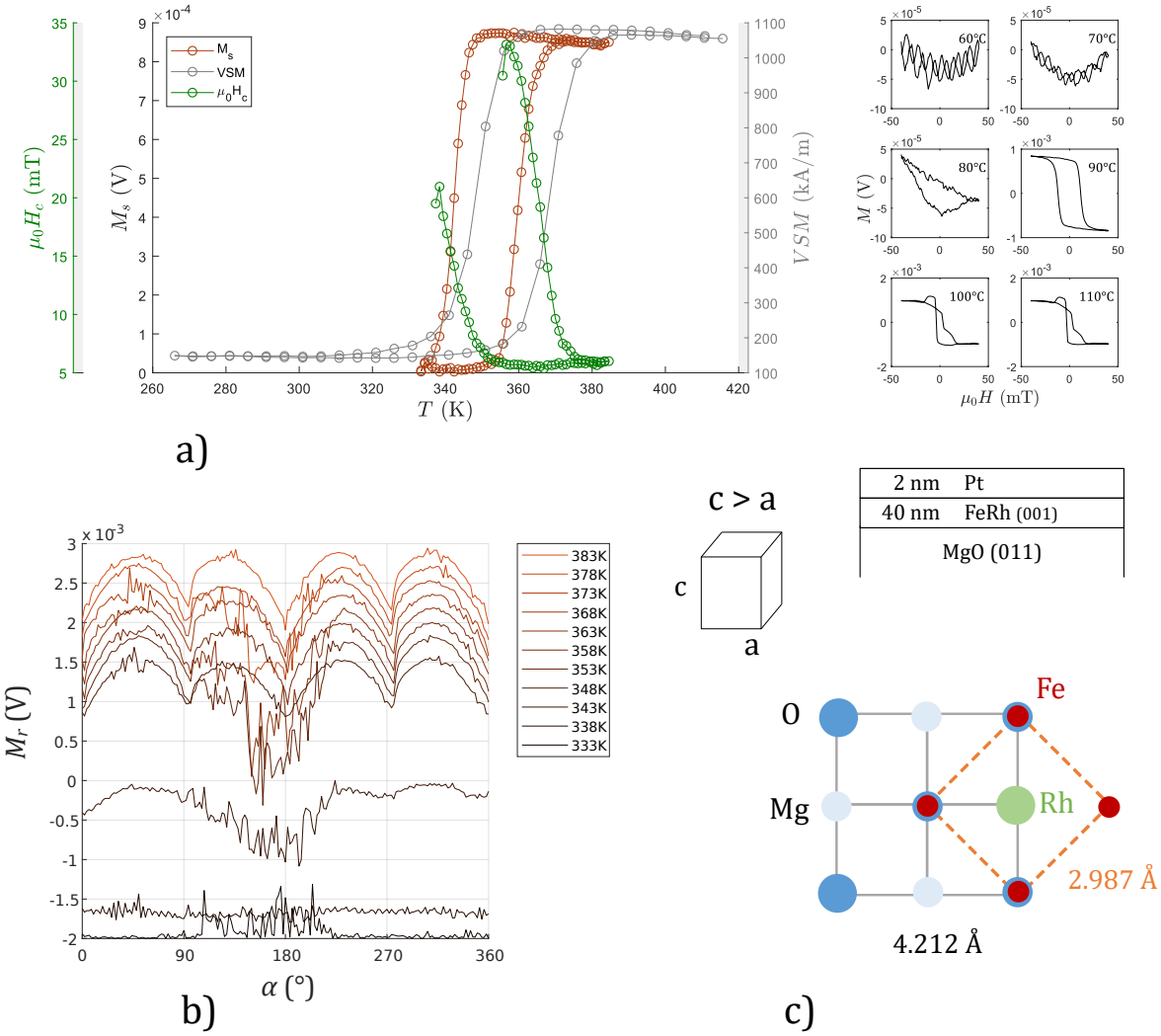

Figure 4.7: a) MOKE measurement of the phase transition and b) anisotropy performed on a 40 nm FeRh layer on an MgO substrate, capped with platinum to prevent oxidation of the iron atoms. The scheme in c) shows the lattice matching of the FeRh with the substrate (courtesy of M.Sc. Jon A. Arregi). The substrate causes the FeRh lattice to expand in the out-of-plane direction.

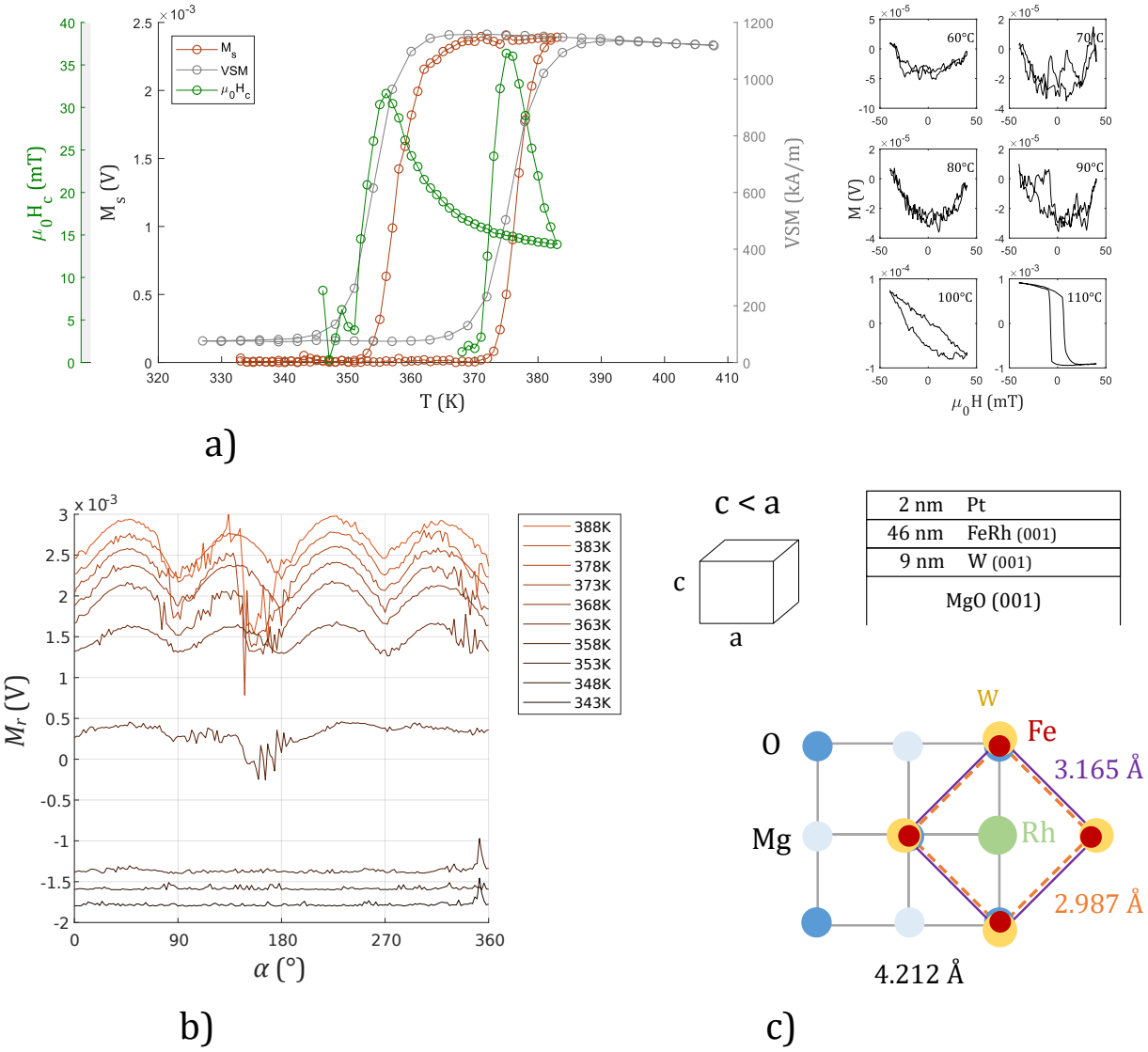

Figure 4.8: a) MOKE measurement of the AF to FM transition and b) anisotropy performed on a 46 nm FeRh layer on an MgO substrate with a tungsten layer. The scheme in c) shows the lattice matching of the FeRh with the substrate (courtesy of M.Sc. Jon A. Arregi). The substrate causes the FeRh lattice to expand in the in-plane direction.

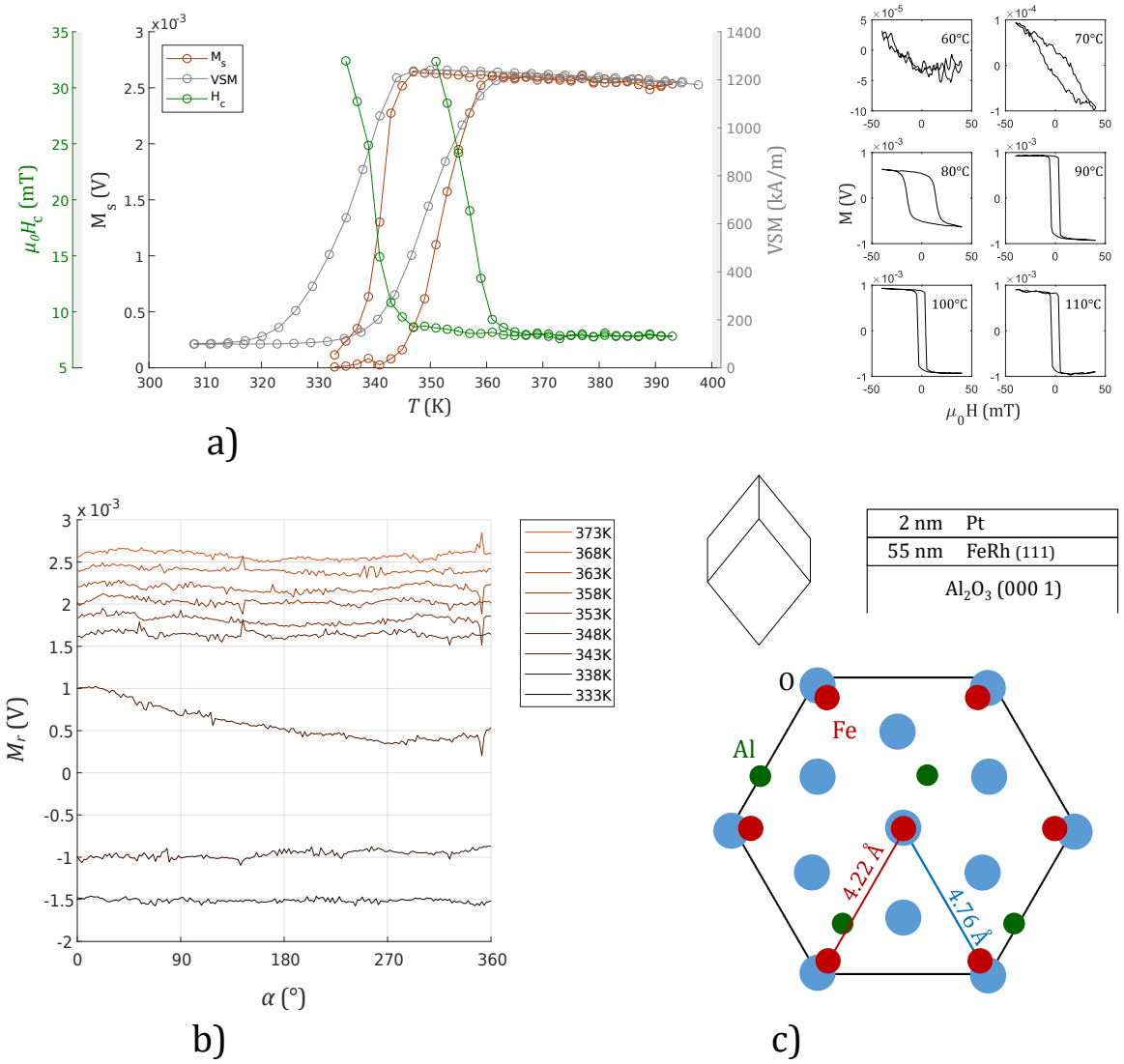

Figure 4.9: a) MOKE measurement of the AF to FM transition and b) anisotropy performed on a 55 nm FeRh layer on a Al_2O_3 substrate. The scheme in c) shows the lattice matching of the FeRh with the substrate (courtesy of M.Sc. Jon A. Arregi). The substrate causes the FeRh lattice to expand out-of-plane.

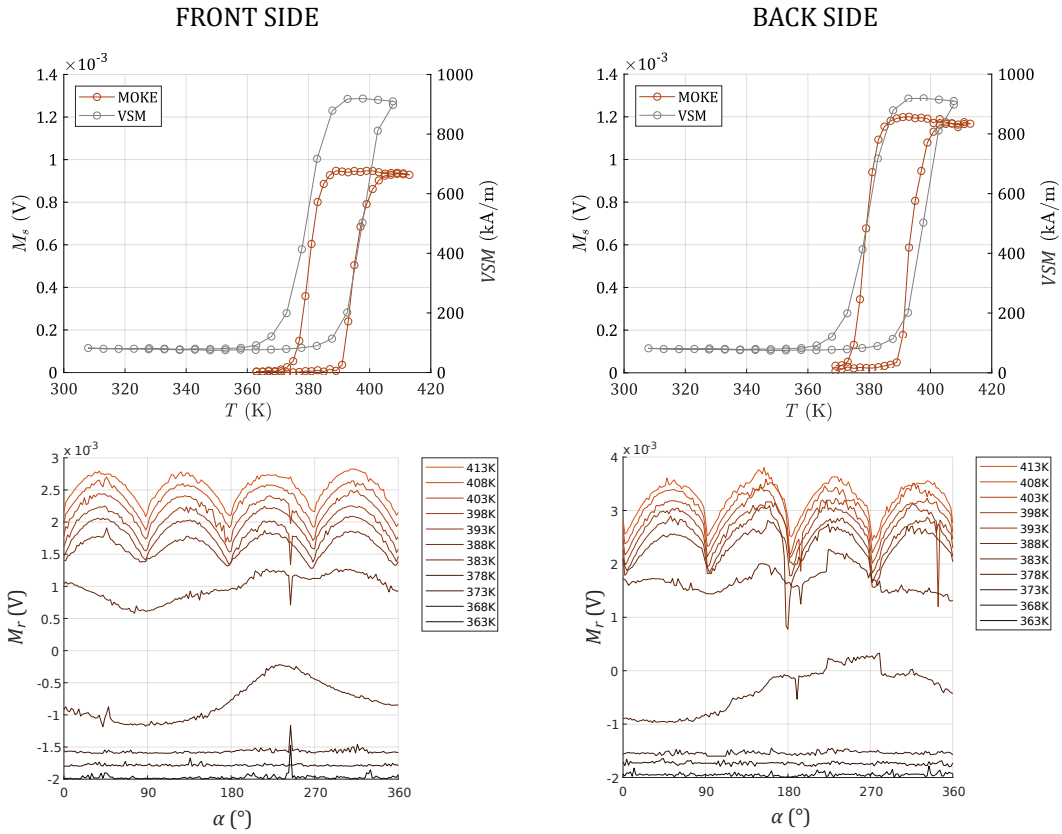

Figure 4.10: Magnetization reversal and anisotropy measurements on a 40-nm-thick FeRh layer deposited on a double polished MgO substrate. The measurements were done from both the front (deposited) and the back (non-deposited) face of the substrate to study the phenomena at the FeRh/MgO boundary. (Difference in the absolute value of the MOKE signal for the front and back side temperature-dependent measurement is probably only caused by the current optical setup alignment.)

Conclusion

In the work presented, we motivate the investigation of spintronic materials with promising applications in non-volatile low-energy data storage and computing. In the theoretical part, it is shown how to deduce the anisotropic properties of metallic layers by controlling the magnetization reversal with an externally applied magnetic field and measuring the magneto-optical response. We introduce the theory of electromagnetism to quantify the interaction of light with a magnetic surface. A functional magneto-optical ellipsometric setup is presented, with an included photoelastic modulator system. Thanks to this component, the setup is able to measure both ellipsometric angles: the Kerr rotation θ_K and ellipticity ϵ_K. Due to the PEM's high-frequency operation, a high signal-to-noise ratio can be obtained by analyzing the detected intensity signal with a lock-in amplifier. An already existing ellipsometric setup was modified to implement the PEM and to allow for automated field-orientation and temperature-dependent measurements. A control software for this modified setup was needed to allow for automated operation, which was programmed in the LabVIEW 2018 environment. A demonstrative measurement was taken on an hcp epitaxial cobalt layer with strong uniaxial anisotropy. By means of the Stoner-Wohlfarth model, we were able to obtain its anisotropy energy coefficients. Subsequently, the FeRh alloy, unique for its temperature-dependent AF to FM phase transition, was inspected. The temperature dependent measurements show a good agreement with the VSM magnetometry data, highlighting the usefulness of magneto-optics to measure the phase transition characteristics. To investigate the effect of substrate-induced epitaxial strain, FeRh layers on three different substrates were measured. For an MgO(001) substrate and also MgO(001) substrate with a thin W(001) buffer layer, the remanent magnetization shows a fourfold anisotropy, while no distinctive anisotropy is observed for an FeRh grown on Al_2O_3(000 1). We were also interested in the phenomena at the FeRh/MgO interface. A new sample with double-side polished MgO substrate was prepared for this purpose. Light was passed through the polished un-deposited substrate side and reflected from the interface, from which we confirmed the existence of a remanent FM phase fraction even at room temperature.

It should be mentioned that an unusually large second-order magneto-optical effect was observed at most of the FeRh layers when measuring with the applied field close to the hard axis. The prospect now is to find a suitable anisotropy energy profile based on Eq. (1.8) to fit the FeRh measurements and also to quantify the second order Kerr effects by means of the second-order permittivity tensor (2.39). Additional interesting experiments could be performed with an out-of-plane applied field or on exchange-coupled adjacent Fe and FeRh layers.

References

[1] JOHNSON, M. and R.H. SILSBEE. Interfacial Charge-Spin Coupling: Injection and Detection of Spin Magnetization in Metals. *Physical Review Letters*. 1985vol. 55, no. 17, pp. 1790–1793. ISSN 0031-9007.

[2] CHAPPERT, C., A. FERT and F.N. VAN DAU. The Emergence of Spin Electronics in Data Storage. In: *Nanoscience and Technology*. Co-Published with Macmillan Publishers Ltd, UK, 2009pp. 147–157. ISBN 978-981-4282-68-0 978-981-4287-00-5.

[3] SINING M. et al. Commercial TMR Heads for Hard Disk Drives: Characterization and Extendibility at 300 Gbit ^{2}. *IEEE Transactions on Magnetics*. 2006vol. 42, no. 2, pp. 97–102. ISSN 0018-9464, 1941-0069.

[4] ENGEL, B.N. et al. A 4-Mb Toggle MRAM Based on a Novel Bit and Switching Method. *IEEE Transactions on Magnetics*. 2005vol. 41, no. 1, pp. 132–136. ISSN 0018-9464.

[5] UMESH, S. and S. MITTAL. A Survey of Spintronic Architectures for Processing-in-Memory and Neural Networks. *Journal of Systems Architecture*. 2018. ISSN 13837621.

[6] WADLEY, P. et al. Electrical Switching of an Antiferromagnet. *Science*. 2016vol. 351, no. 6273, pp. 587–590. ISSN 0036-8075, 1095-9203.

[7] FALLOT, M. and R. HOCART. Sur l'apparition du ferromagnétisme par élévation de température dans des alliages de fer et de rhodium. *Rev. Sci.* 1939vol. 77, pp. 498–500.

[8] QIU, Z.Q. and S.D. BADER. Surface Magneto-Optic Kerr Effect. *Review of Scientific Instruments*. 2000vol. 71, no. 3, pp. 1243–1255. ISSN 0034-6748, 1089-7623.

[9] VISNOVSKY, S. *Optics in Magnetic Multilayers and Nanostructures*. CRC Press, 2006. Optical Science and Engineering. ISBN 9781420019193.

[10] VAVASSORI, P. Polarization Modulation Technique for Magneto-Optical Quantitative Vector Magnetometry. *Applied Physics Letters*. 2000vol. 77, no. 11, pp. 1605–1607. ISSN 0003-6951, 1077-3118.

[11] BLUNDELL, S. *Magnetism in Condensed Matter*. Oxford ; New York: Oxford University Press, 2001. 238 pp. Oxford Master Series in Condensed Matter Physics. ISBN 978-0-19-850592-1.

[12] BROWN, W.F. *Micromagnetics*. Reprint 1978 with corrections. Huntington, N.Y: R. E. Krieger Pub. Co, 1978. 143 pp. ISBN 978-0-88275-665-3.

[13] COEY, J.M.D. *Magnetism and Magnetic Materials*. Cambridge: Cambridge University Press, 2010. 614 pp. ISBN 978-0-511-67743-4. OCLC: 819423378.

[14] FLORCZAK, J.M. and E.D. DAHLBERG. Magnetization Reversal in (100) Fe Thin Films. *Physical Review B*. 1991vol. 44, no. 17, pp. 9338–9347. ISSN 0163-1829, 1095-3795.

[15] STONER, E.C. and E.P. WOHLFARTH. A Mechanism of Magnetic Hysteresis in Heterogeneous Alloys. *Philosophical Transactions of the Royal Society A: Mathematical, Physical and Engineering Sciences*. 1948vol. 240, no. 826, pp. 599–642. ISSN 1364-503X, 1471-2962.

[16] TANNOUS, C. and J. GIERALTOWSKI. The Stoner–Wohlfarth Model of Ferromagnetism. *European Journal of Physics*. 2008vol. 29, no. 3, pp. 475–487. ISSN 0143-0807, 1361-6404.

[17] BUSCH, G. On the History of Magneto-Optics. *Physica B+C*. 1977vol. 89, pp. 1–3. ISSN 03784363.

[18] PARKER, M.R. The Kerr Magneto-Optic Effect (1876–1976). *Physica B+C*. 1977vol. 86-88, pp. 1171–1176. ISSN 03784363.

[19] FLAJŠMAN, L. *Vectorial Kerr Magnetometry*. 2015. 99 pp. [Diplomová práce.] VUT, FSI, Brno.

[20] LEE, K., J. KIM and J. JEONG. Femtosecond Pump-Probe MOKE Microscopy for an Ultrafast Spin Dynamics Study. *Journal-Korean Physical Society*. 2006vol. 49, no. 6, pp. 2402.

[21] STAMM, C. et al. Magneto-Optical Detection of the Spin Hall Effect in Pt and W Thin Films. *Physical Review Letters*. 2017vol. 119, no. 8. ISSN 0031-9007, 1079-7114.

[22] MAXWELL, J.C. *A Treatise on Electricity and Magnetism. Vol. 1: ...* Republ. of 3. ed., Oxford 1891. New York: Dover Publ, 1961. 506 pp. ISBN 978-0-486-60636-1. OCLC: 830833408.

[23] GRIFFITHS, D.J. *Introduction to Electrodynamics*. Cambridge University Press, 2017. 576 pp. ISBN 978-1-108-35714-2.

[24] JACKSON, J.D. *Classical Electrodynamics*. 3rd ed. New York: Wiley, 1999. 808 pp. ISBN 978-0-471-30932-1.

[25] HECHT, E. *Optics*. 4th ed. Adelphi University: Addison-Wesley, 2003. Pearson Education. ISBN 978-0-321-18878-6.

[26] PANCALDI, M. *Study of Geometrical Frustration and Thermal Activation in Arrays of Magnetic Nanostructures*. 2018. University of the Basque Country.

[27] NÝVLT, M. *Magneto-Optical Interactions in Ultrathin Magnetic Film Structures*. 1996. 129 pp. [Dizertační práce.] UK, Praha.

[28] BOAS, M.L. *Mathematical Methods in the Physical Sciences*. Wiley, 2006. ISBN 978-0-471-36580-8.

[29] LANDAU, L. D. et al. *Electrodynamics of continuous media*. 2nd ed., rev. and enl. Oxford [Oxfordshire] ; New York: Pergamon, 1984. 460 pp. Pergamon international library of science, technology, engineering, and social studies. ISBN 978-0-08-030276-8 978-0-08-030275-1.

[30] PERSHAN, P.S. Magneto-Optical Effects. *Journal of Applied Physics*. 1967vol. 38, no. 3, pp. 1482–1490. Available from: doi:10.1063/1.1709678.

[31] VIŠŇOVSKÝ, Š. Magneto-Optical Permittivity Tensor in Crystals. *Czech. J. Phys.* 1986vol. B 36.

[32] FOWLES, G.R. *Introduction to Modern Optics*. Dover Publications, 1989. Dover Books on Physics Series. ISBN 9780486659572.

[33] ARGYRES, P.N. Theory of the Faraday and Kerr Effects in Ferromagnetics. *Physical Review*. 1955vol. 97, no. 2, pp. 334–345. ISSN 0031-899X.

[34] YOU, C.Y. and S.C. SHIN. Generalized Analytic Formulae for Magneto-Optical Kerr Effects. *Journal of Applied Physics*. 1998vol. 84, no. 1, pp. 541–546. ISSN 0021-8979, 1089-7550.

[35] ARREGI, J.A., P. RIEGO and A. BERGER. What Is the Longitudinal Magneto-Optical Kerr Effect? *Journal of Physics D: Applied Physics*. 2017vol. 50, no. 3, pp. 03LT01. ISSN 0022-3727, 1361-6463.

[36] POLISETTY, S. et al. Optimization of Magneto-Optical Kerr Setup: Analyzing Experimental Assemblies Using Jones Matrix Formalism. *Review of Scientific Instruments*. 2008vol. 79, no. 5, pp. 055107. ISSN 0034-6748, 1089-7623.

[37] ARREGI, J. A. et al. Strain-Induced Magneto-Optical Anisotropy in Epitaxial Hcp Co Films. *Physical Review B*. 2015vol. 92, no. 18. ISSN 1098-0121, 1550-235X.

[38] BERGER, A. and M.R. PUFALL. Generalized Magneto-Optical Ellipsometry. *Applied Physics Letters*. 1997vol. 71, no. 7, pp. 965–967. ISSN 0003-6951, 1077-3118.

[39] BERGER, A. and M. R. PUFALL. Quantitative Vector Magnetometry Using Generalized Magneto-Optical Ellipsometry. *Journal of Applied Physics*. 1999vol. 85, no. 8, pp. 4583–4585. ISSN 0021-8979, 1089-7550.

[40] SHTRIKMAN, S. and D. TREVES. On the Resolution of Brown's Paradox. *Journal of Applied Physics*. 1960vol. 31, no. 5, pp. S72–S73. ISSN 0021-8979, 1089-7550.

[41] MAAT, S., J.-U. THIELE and E.E. FULLERTON. Temperature and Field Hysteresis of the Antiferromagnetic-to-Ferromagnetic Phase Transition in Epitaxial FeRh Films. *Physical Review B*. 2005vol. 72, no. 21. ISSN 1098-0121, 1550-235X.

[42] ARREGI, J.A. et al. Magnetization Reversal and Confinement Effects across the Metamagnetic Phase Transition in Mesoscale FeRh Structures. *Journal of Physics D: Applied Physics*. 2018vol. 51, no. 10, pp. 105001. ISSN 0022-3727, 1361-6463.

[43] BALDASSERONI, C. et al. Temperature-Driven Nucleation of Ferromagnetic Domains in FeRh Thin Films. *Applied Physics Letters*. 2012vol. 100, no. 26, pp. 262401. ISSN 0003-6951, 1077-3118.

[44] BORDEL, C. et al. Fe Spin Reorientation across the Metamagnetic Transition in Strained FeRh Thin Films. *Physical Review Letters*. 2012vol. 109, no. 11. ISSN 0031-9007, 1079-7114.

[45] HAMRLE, J. et al. Huge Quadratic Magneto-Optical Kerr Effect and Magnetization Reversal in the Co $_2$ FeSi Heusler Compound. *Journal of Physics D: Applied Physics*. 2007vol. 40, no. 6, pp. 1563–1569. ISSN 0022-3727, 1361-6463.

[46] FAN, R. et al. Ferromagnetism at the interfaces of antiferromagnetic FeRh epilayers. *Phys. Rev. B*. 2010vol. 82, pp. 184418.

List of abbreviations

AF	antiferromagnetic
EA	easy axis
FM	ferromagnetic
GME	generalized magneto-optical ellipsometry
MOKE	magneto-optical Kerr effect
PEM	photoelastic modulator
QWP	quaterwave plate
SW	Stoner-Wohlfarth model
VSM	vibrating sample magnetometry

A. Stoner-Wohlfarth model

There is an effective way to compute the dependance $\theta^*(H)$ iteratively using a computer. It is called *the effective field method*. It introduces the effective field $\boldsymbol{H}_{eff}$ that is a fictional field that acts on the magnetized particle and it substitutes all the possible effects expressed in the total energy E. It is therefore implicitly defined by E as

$$\begin{aligned} E &= -\mu_0 \boldsymbol{M} \cdot \boldsymbol{H}_{eff} \\ &= -\mu_0 (M_x H_{eff,x} + M_y H_{eff,y}) \,. \end{aligned} \tag{A.1}$$

Because the EA corresponds to the x-axis, the direction cosines of $\boldsymbol{M}$ read:

$$\begin{aligned} m_x &= \cos\theta \,, \\ m_y &= \sin\theta \,. \end{aligned} \tag{A.2}$$

From (A.1) it follows that

$$\begin{aligned} H_{eff,x} &= -\frac{1}{\mu_0 M_s} \frac{\partial E}{\partial m_x} \,, \\ H_{eff,y} &= -\frac{1}{\mu_0 M_s} \frac{\partial E}{\partial m_y} \,, \end{aligned} \tag{A.3}$$

where we used $M_x = M_s m_x$, $M_y = M_s m_y$.

We substitute to (A.3) from (1.6) and make use of (A.2). It follows that

$$\begin{aligned} H_{eff,x} &= H_{Ku} m_x + H \cos\alpha \\ H_{eff,y} &= H \sin\alpha \,, \end{aligned} \tag{A.4}$$

It follows from (A.1) that, in order for the energy to be minimized, the magnetization will eventually align with H_{eff} - the direction of $\boldsymbol{H}_{eff}$ and $\boldsymbol{M}$ are the same:

$$\begin{aligned} m_x &= \frac{H_{eff,x}}{\sqrt{H_{eff,x}^2 + H_{eff,y}^2}} \\ m_y &= \frac{H_{eff,y}}{\sqrt{H_{eff,x}^2 + H_{eff,y}^2}} \,. \end{aligned} \tag{A.5}$$

These are self-consistent equations that can be used for an iterative computation of m_x, m_y. Starting from the negative saturation, we can use an initial guess $m_x = -\cos\alpha \,, m_y = = -\sin\alpha$.